JOURNAL OF PETROLOGY | VOLUME 42 | NUMBER 2 | PAGES 433–457 | 2001

Age, Geochemistry and Petrogenesis of the Ultramafic Pipes in the Ivrea Zone, NW Italy

G. GARUTI[1]*, F. BEA[2], F. ZACCARINI[3] AND P. MONTERO[2]

[1]DEPARTMENT OF EARTH SCIENCES, UNIVERSITY OF MODENA, ST EUFEMIA 19, MODENA 41100, ITALY

[2]DEPARTMENT OF MINERALOGY AND PETROLOGY, UNIVERSITY OF GRANADA, CAMPUS FUENTENUEVA, 18002 GRANADA, SPAIN

[3]DEPARTMENT OF EARTH SCIENCES AND ENVIRONMENTAL GEOLOGY, UNIVERSITY OF BOLOGNA, PIAZZA DI PORTA S. DONATA 1, I-40126 BOLOGNA, ITALY

RECEIVED JUNE 22, 1999; REVISED TYPESCRIPT ACCEPTED JUNE 2, 2000

Pipe-like ultramafic bodies, hosting Ni–Cu–PGE sulphide deposits, intrude the Main Gabbro and the roof metasediments of the Ivrea Zone, NW Italy. These bodies were emplaced at 287 ± 3 Ma and represent the last mantle-derived melts associated with an underplating event that largely drove the crustal evolution of this area during the late Carboniferous (~300–290 Ma). The pipes are composed of volatile-rich ultramafic rocks and gabbros with an alkaline signature simultaneously enriched in both incompatible and the most compatible elements but depleted in elements of intermediate compatibility. The isotope composition of these pipe rocks is $\varepsilon_{290\,Ma}(Nd)$ *~3·7 to −1·9 and* $\varepsilon_{290\,Ma}(Sr)$ *~0·8–26. In a* $\varepsilon_{290\,Ma}(Nd)$ *vs* $\varepsilon_{290\,Ma}(Sr)$ *diagram they define a linear array between the un-metasomatized and metasomatized peridotites of Finero, but distinctly oblique with respect to the trend defined by Balmuccia peridotites. The* $\delta^{34}S$ *ranges from 0·0 to +0·9‰ and is indicative of a mantle source. We suggest that the pipes represent infiltration of melts derived from a depleted mantle protolith flushed with alkaline metasomatic fluids, probably of juvenile mantle origin, which underwent partial melting as a consequence of the depression of the solidus owing to the increased activity of water and other volatiles. The similarity in age, trace-element, and isotopic signatures indicates that the pipes were probably produced in the course of the same metasomatic event that affected the Finero ultramafic body. The overall geochemical characteristics of the pipes are more consistent with magmatism related to a mantle plume than with a subduction setting.*

KEY WORDS: *Basic Complex; Ivrea Zone; mantle plume; underplating; zircon age*

INTRODUCTION

The Ivrea Zone, in NW Italy, is believed to represent an exposed section of the lower continental crust (Mehnert, 1975; Garuti *et al.*, 1980; Percival *et al.*, 1992) whose evolution has been largely driven by the underplating of mantle-derived basic magmas (the Basic Complex), associated with the uplift of large fragments of mantle peridotites (the Mantle Tectonite massifs of Baldissero, Balmuccia and Finero), beneath the metamorphic basement of the Southern Alps (the Kinzigitic Formation) (Fig. 1). Although this area has been the object of numerous studies that have significantly contributed to the understanding of the evolution of the lower continental crust [see Percival *et al.* (1992) and references therein], many aspects of the underplating process, especially the timing of emplacement of basic magmas and whether the environment was a mantle plume (e.g. Shervais & Mukasa, 1991) or a subduction setting (e.g. Hartmann & Wedepohl, 1993; Zanetti *et al.*, 1999), are still unresolved.

A particularly striking group of intrusions, whose study may be relevant for understanding the geodynamic setting and evolution of the Ivrea Zone, consists of pipe-like bodies formed of amphibole-rich peridotites and pyroxenites with minor hornblendites and gabbros, anomalously rich in volatiles and incompatible elements, which were emplaced into either the upper part of the Basic Complex or the overlying Kinzigitic Formation

*Corresponding author. Telephone: +39-059-417225. Fax: +39-059-417399. E-mail: garutig@unimo.it

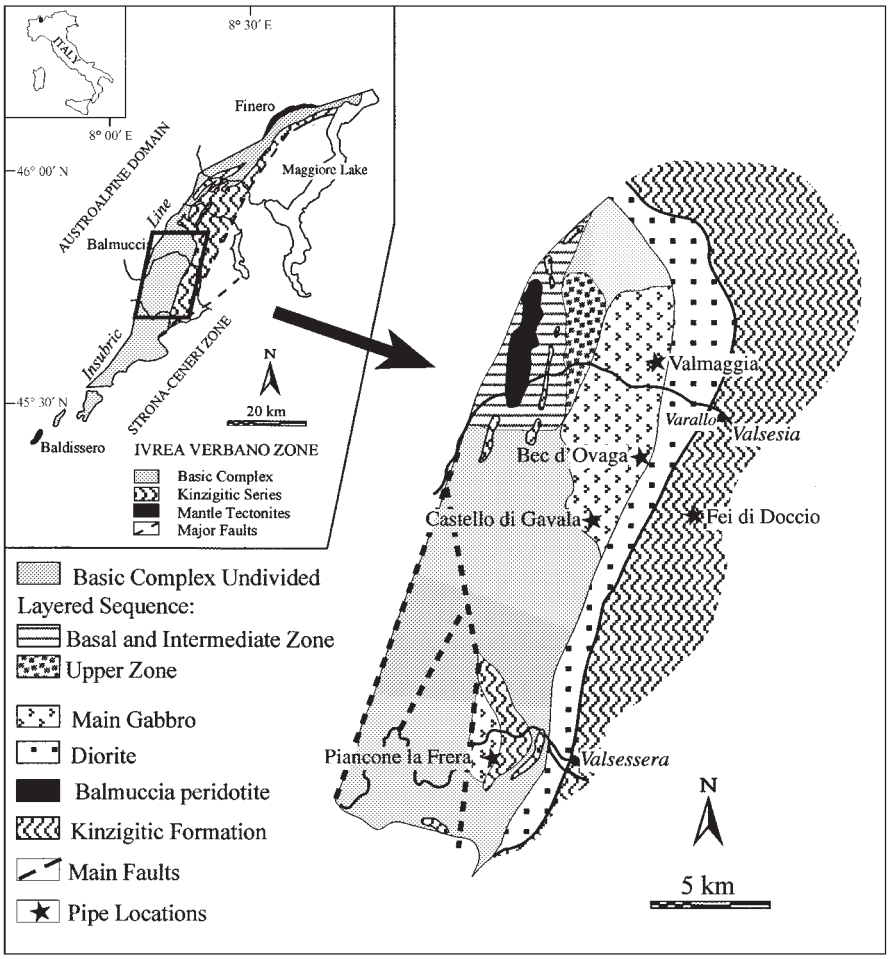

Fig. 1. Geological sketch of the Ivrea Zone, showing a general subdivision of the units in the area between Valsesia and Valsessera. The location of the ultramafic pipes of Valmaggia, Bec d'Ovaga, Castello di Gavala, Fei di Doccio and Piancone la Frera is shown.

(Ferrario *et al.*, 1982; Garuti *et al.*, 1986). These rocks are well known among metallogenists because of their workable Ni–Cu sulphide deposits (Huttenlocher, 1934; Bertolani, 1952), but have been rarely studied by petrologists, despite the fact that they might represent the last mantle-derived melts associated with the underplating event.

This paper presents petrographic, geochemical and isotopic data aimed at understanding the petrogenesis of the ultramafic pipes. We studied their major-element, trace-element (including REE, Au and Pt-group elements), and Sr and Nd isotope composition, and dated them, together with a host diorite, with the single-zircon $^{207}Pb/^{206}Pb$ stepwise-evaporation method. On the basis of these data, we suggest the existence of an ultrabasic magmatism with alkaline affinities that closely followed the emplacement of the Basic Complex in the central Ivrea Zone. We discuss the origin of this magmatism and its bearing on geodynamic setting and nature of the mantle source, especially whether it is consistent with a mantle plume or a subduction environment.

GEOLOGICAL BACKGROUND

The Ivrea Zone is sigmoidal in shape, extending over about 160 km × 20 km. It is limited by major regional faults: the Insubric line to the W and NW, which separates the Ivrea Zone from the Austroalpine Domain, and the Cremosina, Cossato–Mergozzo–Brissago and Pogallo lines to the south and SE, which separate the Ivrea Zone from the Strona–Ceneri Zone (Boriani *et al.*, 1990) (Fig. 1). As in the rest of the Southern Alps, there is no Tertiary metamorphic overprint characteristic of the Alpine domains.

The Ivrea Zone is composed of three formations, the Mantle Tectonites, the Basic Complex and the Kinzigite Formation. The Basic Complex is formed of a variety of

gabbros and diorites (Garuti *et al.*, 1980; Pin & Sills, 1986; Sinigoi *et al.*, 1994). The Mantle Tectonites occur inside the Basic Complex as medium-sized massifs along the Insubric line at the localities of Baldissero, Balmuccia and Finero. They are considered to be obducted fragments of subcontinental mantle showing variable degrees of extraction of partial melts and metasomatism (Hartmann & Wedepohl, 1993). The Finero massif, in particular, displays the effects of metasomatism by water-rich fluids that caused the reintroduction of incompatible elements into a depleted mantle protolith, inducing extensive crystallization of phlogopite and amphibole. The Kinzigite Formation is structurally located above the Basic Complex. It consists of a prograde metamorphic sequence of metapelites (*sensu lato*, i.e. quartz-bearing peraluminous metasediments) and felsic meta-volcanic rocks with minor intercalations of meta-basic igneous rocks, quartzites and marbles. These rocks are metamorphosed from middle amphibolite to granulite facies, the metamorphic gradient increasing towards the Basic Complex, so that in the granulite zone they underwent intense partial melting and melt segregation (Schnetger, 1994; Bea & Montero, 1999).

In the Valsesia area of the central Ivrea Zone, the Basic Complex consists of three units: the Layered Series, the Main Gabbro and the Diorites. The Layered Series, also known as the Cyclic Units, is a sequence of layered mafic–ultramafic rocks that contains irregularly intercalated septa of strongly migmatized metasediments. The Main Gabbro and the Diorites are rarely layered, but both have a NE–SW foliation, apparently determined by syn-magmatic stretching and deformation. The contact between the Layered Series and the Main Gabbro is marked by faults and a prominent metasedimentary septum up to 100 m thick, suggesting that the two formations probably represent separate intrusive events (Ferrario *et al.*, 1982). The contact between the Main Gabbro and the Diorites is either faulted or transitional, in the latter case being caused by the gradual increase in modal biotite and the appearance of quartz. The roof of the Diorites unit is in magmatic contact with the metasediments of the Kinzigite Formation.

FIELD RELATIONSHIPS

The ultramafic pipes occur as small ($\varphi_{max} \sim$ 50–300 m) discordant intrusive bodies emplaced either into the Main Gabbro of Valsesia, at the localities of Valmaggia, Bec d'Ovaga and Castello di Gavala, or into the metapelites and marbles of the Kinzigite Formation, at Fei di Doccio (Fig. 1). So far, they have not been found inside the Layered Series or in other mafic–ultramafic units of the Basic Complex. Only one discordant pyroxenite body with petrographic and metallogenetic features similar to the pipes has been found intruding the Main Gabbro of Valsessera, at the locality of Piancone la Frera (Bertolani *et al.*, 1980; Garuti *et al.*, 1986). Other pyroxenite dykes with associated sulphide mineralization occur in other localities of the Ivrea Zone, but their petrographic and metallogenetic features are not comparable with the pipes discussed in this paper.

The pipes are not well exposed, their geometry and relationship with the host rocks being visible only in underground mining works. The pipes are usually massive, with no layering or cumulus structures. The ultramafic lithologies may locally grade into plagioclase-rich pyroxenites and olivine gabbros that form small ($\sim$0·5–2 m) irregular bodies within the pipes. Pegmatoid pods and veins, from a few centimetres up to 1 m wide, of amphibole plagioclasite to plagioclase hornblendite occur in the peripheral zones. The contacts with host rocks are sharp. In some localities, the host gabbros show a metasomatic aureole up to several metres wide enriched in biotite, titanite, apatite, zircon and sulphides. In a few cases, the pipe is also metasomatized near the contact, so that it was transformed into a massive intergrowth of light green hornblende, sericite, tremolite, chlorite, and carbonates, surrounding partially serpentinized olivine and other relics of the primary silicates.

SAMPLES AND METHODS

Samples

Approximately 100 samples from the pipes were examined in thin section, 26 of which were selected for detailed petrological and geochemical studies. Care was taken to cover all the lithological variations displayed by the pipes, but samples affected by late-stage deuteric alteration were discarded. A subset of nine samples, one from Piancone la Frera and two from each of the other pipes, were also analysed for Sr and Nd isotopes (whole rock). One zircon-rich sample from Bec d'Ovaga and one from Fei di Doccio were used for zircon dating. The location and type of the samples studied are summarized in Table 1. Most of the samples from Fei di Doccio and the one from Piancone la Frera were collected from mining dumps, because of the poor exposure of the pipes at both localities and the impossibility of entering the old mines. Two separate pyroxenite bodies were sampled at Valmaggia, and are defined as the 'main' and the 'small' body in Table 1. Sample VM140B is a pyroxenite at the transition with a gabbroic pod at the margin of the main body. Sample GV1232 from Castello di Gavala is the metasomatized and mineralized wall rock of the pipe.

Microprobe analysis

Electron microprobe analyses were carried out at the University of Modena using an ARL-SEMQ instrument

Table 1: Location and petrography of the studied pipe rocks

Sample	Lithology	Location	Mineral assemblages		
			Main	Accessory	Opaques
Bec d'Ovaga					
BO1	Px	core	Hbl–Ol–Opx–Cpx–Phl	Pl–Spl–Ap–Cb	Sf–Ilm–Mag
BO6	Gb	pod in the core	Pl–Hbl–Opx–Cpx–Phl	Ap–Zm	Sf–Ilm
BO9	Px	core	Hbl–Ol–Opx–Cpx–Phl	Pl–Spl–Ap	Sf–Ilm–Mag
BO1250	Px	(1 m from NW contact)	Hbl–Ol–Opx–Cpx	Phl–Pl–Spl–Ap–Zm	Sf–Ilm–Rt
BO1253	Px	(1 m from SE contact)	Hbl–Ol–Opx–Cpx–Phl	Ap–Cb–Zm	Sf–Ilm
BO1258	Plg	core	Pl–Hbl–Bt	Zm–Ap	—
BO1272	Px	core	Hbl–Opx–Cpx–Phl	Ol–Pl–Spl–Ap–Zm	Sf–Ilm–Rt
Fei di Doccio					
FD1	Px	dump	Hbl–Ol–Cpx–Opx	Pl–Phl–Spl–Ap–Zm–Bd	Sf–Ilm–Rt–Mag–Gr
FD2	Px	dump	Ol–Cpx–Hbl	Spl–Chl–Spr	Sf–Ilm
FD3	Horn	dump	Hbl–Tr	Spl–Chl–Cb–Bt	Sf
FD4	Px	1 m from S contact	Hbl–Ol–Cpx–Phl	Spl–Cb	Sf–Ilm
FD5	Mp	in contact with FD4	Qtz–Hbl–Bt–Kfs–Pl	Cb–Sil	Sf
FD6	Px	10 m from S contact	Hbl–Ol–Opx–Cpx–Phl	Pl–Spl–Ap–Cb	Sf–Gr–Ilm–Mag
Castello di Gavala					
GV1224	Gb	marginal pod	Pl–Opx–Cpx–Hbl	Bt–Ap	Sf
GV1228	Gb	marginal pod	Pl–Opx–Cpx–Hbl	Bt–Ap–Zrn	Sf
GV1230	Px	core	Hbl–Opx–Ol	Spl–Phl–Ap–Cb	Sf–Ilm–Mag
GV1232	Gb–Dior	wall rock	Pl–Cpx–Opx	Bt–Ap–Hbl–Tit	Sf–Ilm
GV1235	Gb	marginal pod	Pl–Opx–Cpx–Hbl	Bt	Sf
GV1262	Px	core	Hbl–Opx–Ol	Spl–Phl–Ap–Cb	Sf–Ilm
GV1279	Px	dump	Hbl–Cpx–Opx–Ol	Spl–Phl	Sf–Ilm–Mag
Valmaggia					
VM1	Px	core main body	Hbl–Ol–Opx–Cpx	Pl–Spl–Ap–Cb–Phl	Sf–Ilm–Mag
VM3	Px	core main body	Hbl–Ol–Opx–Cpx	Pl–Spl–Ap–Cb	Sf–Mag
VM140B	Px	margin main body	Hbl–Cpx–Ol	Pl–Spl–Phl	Sf–Mag
VM1326	Px	core small body	Hbl–Ol–Opx–Cpx	Spl–Phl–Ap	Sf–Ilm–Rt–Mag
VM1327	peg–Gb	pod in the core	Pl–Hbl–Opx	Spl–Ap–Tit	Sf–Ilm–Mag
VM1328	peg–Gb	pod in the core	Pl–Hbl–Opx	Ap	Sf
VM1329	Px	margin small body	Hbl–Ol–Opx–Cpx	Phl–Spl–Cb	Sf–Ilm–Mag–Hem
Piancone la Frera					
PC1220A	Px	dump	Opx–Cpx–Hbl	Ol–Spl	Sf

Px, pyroxenite; Gb, gabbro; Plg, plagioclasite; Dior, diorite; peg-Gb, pegmatoid gabbro; Horn, hornblendite; Mp, metapelite; Ol, olivine; Opx, orthopyroxene; Cpx, clinopyroxene; Hbl, hornblende; Pl, plagioclase; Phl, phlogopite; Spl, spinel; Bt, biotite; Ap, apatite; Zrn, zircon; Bd, baddeleyite; Cb, carbonates; Tit, titanite; Tr, tremolite; Chl, chlorite; Qtz, quartz; Kfs, K-feldspar; Sil, sillimanite; Spr, serpentine; Sf, sulphide; Ilm, ilmenite; Rt, rutile; Mag, magnetite; Hem, hematite; Gr, graphite.

operated at 15 kV accelerating voltage and 20–10 nA beam current, with a beam diameter of ~1 μm, and counting times of 20 and 5 s for peak and backgrounds, respectively. On-line data reduction was performed with the PROBE software, using natural olivine, clinopyroxene, biotite, chromite, ilmenite, spessartine, apatite and the pure metals Ni, Zn and V as standards. Fluorine and chlorine were standardized on fluorite and tugtupite ($Na_4BeAlSi_4O_{12}Cl$, containing 7·58 wt % Cl), respectively. The analyses of La, Ce, Pr, Nd, Y, Hf and

Zr were calibrated on synthetic silicates and oxides. The observed interferences P–F, Ce–Nd and La–P were corrected automatically. Detection limits were usually in the range of 0·1–0·05% for major and trace elements under routine analysis conditions. Detection limits as low as 0·03% and 0·015% were obtained for F, Cl and the trace elements La, Ce, Pr, Nd, Y, Hf and Zr by choosing suitable counting times and accelerating voltage to improve peak/background ratios.

Whole-rock major- and trace-element analyses

Whole-rock analyses were carried out at the University of Granada. Major elements were determined by X-ray fluorescence (XRF) after fusion with lithium tetraborate. Typical precision was better than $\pm 1{\cdot}5\%$ for an analyte concentration of 10 wt %. Zr, Cr and S were determined by XRF on pressed pellets, with a precision better than $\pm 4\%$ for 100 ppm of Zr and Cr, and $\pm 10\%$ for S concentrations in the range of 0·05–2·5 wt %. Sulphide-mineralized samples with S contents above 2·5 wt % were diluted with increasing amounts of pure silica to bring them within the analytical scale range. PGE and Au were analysed by instrumental neutron activation analysis (INAA) after a nickel-sulphide button pre-concentration step [see Garuti *et al.* (1990) for source of data and analytical details]. Trace elements were determinated by inductively coupled plasma mass spectrometry (ICP-MS) after HNO_3 + HF digestion of 0·1000 g of sample powder in a Teflon-lined vessel at $\sim$180°C and $\sim$200 p.s.i. ($2{\cdot}9 \times 10^4$ Pa) for 30 min, evaporation to dryness, and subsequent dissolution in 100 ml of 4 vol. % HNO_3. Instrument measurements were carried out in triplicate with a PE SCIEX ELAN-5000 spectrometer using Rh as internal standard. Precision was better than $\pm 2\%$ and $\pm 5\%$ for analyte concentrations of 50 and 5 ppm, respectively.

Isotope analyses

Samples for Sr and Nd isotope analyses were digested in the same way using ultra-clean reagents, and analysed by thermal ionization mass spectrometry (TIMS) in a Finnigan Mat 262 spectrometer after chromatographic separation with ion exchange resins. Normalization values were $^{86}Sr/^{88}Sr = 0{\cdot}1194$ and $^{146}Nd/^{144}Nd = 0{\cdot}7219$. Blanks were 0·6 and 0·09 ng for Sr and Nd, respectively. The external precision (2σ), estimated by analysing 10 replicates of the standard WS-E (Govindaraju *et al.*, 1994), was better than 0·003% for $^{87}Sr/^{86}Sr$ and 0·0015% for $^{143}Nd/^{144}Nd$. $^{87}Rb/^{86}Sr$ and $^{147}Sm/^{144}Nd$ were directly determined by ICP-MS following the method developed by Montero & Bea (1998), with a precision better than 1·2% and 0·9% (2σ), respectively.

Sulphur isotope compositions ($\delta^{34}S$) of selected samples were analysed on $\sim$200 mg of bulk sulphide concentrates by mass spectrometry at the Geochronology Laboratory Division of Krueger Enterprises Inc. (Cambridge, MA, USA). Analytical precision and overall accuracy declared by the supplier are better than $\pm 0{\cdot}02\%$ and $\pm 0{\cdot}05\%$, respectively.

Single-zircon $^{207}Pb/^{206}Pb$ stepwise-evaporation analyses were performed at the University of Granada following the method developed by Kober (1986, 1987). Zircon grains were mounted on canoe-shaped Re evaporation filaments and heated until the lead beam was intense enough ($\sim$200–400 ^{206}Pb ions/s). Lead was collected on the ionization filament for 20–30 min, then analysed in five blocks with seven scans per block. Once the analysis was finished, a new evaporation step was started by heating the zircon on the evaporation filament at a higher temperature than in the previous step (usually increasing the current by 50–100 mA) and analysing on the ionization filament as before. The procedure was repeated until all the lead was exhausted from the zircon. The number of steps depended on the size and lead content of each zircon. Data acquisition was performed in dynamic mode (peak hopping), using a secondary electron multiplier as detector with the 206–204–206–207–208 mass sequence. The mass ratio 204/206 was monitored to detect and, if necessary, correct for common lead. Factors for common lead correction were calculated by iteration from the $^{204}Pb/^{206}Pb$ and $^{204}Pb/^{207}Pb$ ratios provided by the model of Stacey & Kramers (1975) at the calculated age, until convergence to a constant value. Mass fractionation caused by the sequential reading of isotopes in a single detector was corrected by multiplying by $\sqrt{(207/206)}$. Standard errors for each step were calculated according to the formula $SE = 2\sigma/\sqrt{n}$. However, the 2σ confidence interval for the final age is given by $[X - t(0{\cdot}025)\sigma/\sqrt{n},\ X + t(0{\cdot}005)\sigma/\sqrt{n})]$, where X and σ are the average and the standard deviation of measured steps, n is the number of steps, and $t(0{\cdot}025)$ is the upper (0·025) point of the t distribution for $n - 1$ degrees of freedom (see Johnson & Bhattacharyya, 1984, p. 296).

PETROGRAPHY AND MINERALOGY

Macroscopically, the pipes appear as massive, dark grey rocks with a coarse (up to 1–1·5 cm), equigranular to heterogranular texture. They are mainly composed of olivine, pyroxenes, Ti-rich brown amphibole, sulphide nodules ($\sim$0·5–2 cm) and discrete amounts of interstitial plagioclase, with minor phlogopite and green spinel. The amphibole appears either as large poikilitic crystals including rounded or skeletal crystals of olivine and

pyroxene, or as an interstitial network of interlocked crystals that surround zones dominated by olivine and pyroxenes. Coronitic textures, frequent in both pyroxenites and gabbros, have olivine at the core, with a sequence of concentric rims of orthopyroxene, amphibole–clinopyroxene and amphibole–spinel symplectite in contact with plagioclase. Phlogopite is usually associated with amphibole and in some cases replaces olivine.

The major mineral assemblage is always accompanied by a complex association of accessory phases consisting of Fe–Ti oxides (rutile, ilmenite, magnetite), apatite, zircon, rare baddeleyite, titanite, carbonates, graphite and minute crystals of barite. Zircon and titanite are mainly found associated with phlogopite and, less frequently, with amphibole. Apatite may be locally abundant and form crystals up to 1 mm long; it appears either associated with plagioclase or as inclusions in amphibole and phlogopite together with euhedral crystals of carbonates.

Sulphide and PGE minerals

Sulphide nodules are present in both ultramafic and gabbroic facies of the pipes, typically associated with amphibole and phlogopite. Their morphology, mode of occurrence and, especially, the fact that they are also locally found as inclusions in olivine, suggest that the sulphide was segregated as droplets of immiscible liquid from the silicate melt at a high-temperature stage owing to a sharp decrease in S solubility (Garuti *et al.*, 1986). The random distribution and variable size of the nodules give no evidence for gravitative settling. In some cases, the sulphide appears to have been mobilized and redeposited along fissures and veins during the late deuteric stage, producing local enrichments and even fairly massive sulphide ores.

Sulphide mineralogy is dominated by the magmatic assemblage pyrrhotite, pentlandite and chalcopyrite, with minor pyrite, cubanite and mackinawite, and with molybdenite, sphalerite, cobaltite, gersdorffite and graphite as accessory phases. Pt–Pd-rich melonite ($NiTe_2$) and rare merenskyite ($PdTe_2$) are the main PGE-bearing minerals in the pipes. Irarsite (IrAsS) has also been found locally (Garuti & Zaccarini, 1994). The presence of a variety of tellurides, hessite (Ag_2Te), altaite (PbTe) and pilsenite (BiTe), along with bismuthinite (Bi_2S_3) and the Au–Ag alloy electrum distinguishes the sulphide deposits in these pipes from those in the Basic Complex, which apparently contain only Ni, Pd and Pt tellurides (Garuti & Rinaldi, 1986).

MINERAL CHEMISTRY

Silicates

Representative compositions of major phases are listed in Tables 2–6. Compositions of olivine and orthopyroxene are in the ranges Fo ~70–85 and En ~70–82, respectively, showing a decrease in the Mg/Fe ratio from ultramafic to gabbroic rocks. Both minerals contain amounts of Mn (MnO ~0·15–0·45 wt % in olivine, and 0·11–0·99 wt % in orthopyroxene) that usually increase with decreasing Mg/(Fe + Mg). Orthopyroxene has rather low CaO, usually in the range 0·2–1·6 wt %. The Ni content of olivine varies irregularly between NiO ~0·15 and 0·30 wt %, showing no clear correlation with the forsterite content. Most olivine grains are zoned with respect to Ni, whose concentration at the rims drops below the microprobe detection limit when they are in contact with interstitial sulphides. Clinopyroxene has a fairly restricted composition, $Wo_{45–50}Fs_{5–14}En_{40–49}$, whereas minor elements vary, Al_2O_3 ~3·56–4·65 wt %, Na_2O ~1·06–1·65 wt %, TiO_2 ~0·40–0·88 wt %, MnO ~0·12–0·24 wt %, and K_2O up to 0·25 wt %. The composition of amphibole ranges from pargasite to kaersutitic pargasite characterized by Mg/(Mg + Fe) ~0·60–0·87, Na + K (a.f.u.) ~0·75–1·68, and elevated Ti contents, up to TiO_2 ~4·54 wt %. Variable amounts of F (up to 0·25 wt %) and Cl (up to 0·05 wt %) have been detected. The F content and the K/Na ratio in the A-site of pargasite correlate positively, and both decrease with increasing Mg/(Fe + Mg). Phlogopite has a range in Mg and Fe contents similar to amphibole and varies in composition from Na rich and Ti poor (Na_2O ~3·15 wt %, TiO_2 ~0·77 wt %) to Na poor and Ti rich (Na_2O ~0·34 wt %, TiO_2 ~6·45 wt %) with decreasing Mg/(Fe + Mg). Phlogopite has F up to 0·35 wt % and Cl up to 0·08 wt %, slightly higher than amphibole. Plagioclase ranges in composition from An_{47} to An_{69}, and usually contains <0·3 wt % K_2O, although lamellae of almost pure K-feldspar are encountered along the cleavage planes of phlogopite.

Non-silicates

Apatite is characterized by high F and Cl contents, which vary reciprocally with a roughly negative correlation. Two groups can be distinguished, fluorapatite with F (0·53–3·84 wt %) > Cl (0·37–0·88 wt %) and chlorapatite with Cl (1·40–2·37 wt %) > F (0·47–1·34 wt %). The two types are found within the same sample, showing no obvious correlation with grain size, mineral assemblage or textural position. Apatite is the major carrier of light rare earth elements (LREE), which are commonly present up to concentrations of Ce_2O_3 ~0·29 wt %, La_2O_3 ~0·19 wt %, Nd_2O_3 ~0·40 wt %, and Pr_2O_3 ~0·53 wt %. Detailed microprobe study of some large

Table 2: Selected microprobe analyses of olivine and orthopyroxene

Sample:	BO1	BO9	FD1-1	FD1-2	FD4	GV1230	GV1262	GV1279	VM1	VM140B-1	VM140B-2	PC1220A
Rock type:	Px	Px	Px	Px	Px	Px	Px	Px	Px	Px	Gb	Px
Olivine												
SiO_2	39·35	37·80	36·85	38·62	39·26	38·51	38·99	39·35	38·61	38·01	36·10	39·89
TiO_2	0·00	0·00	0·00	0·02	0·04	0·00	0·00	0·06	0·02	0·00	0·00	0·00
Al_2O_3	0·00	0·00	0·00	0·00	0·00	0·06	0·01	0·00	0·00	0·00	0·00	0·02
FeO	14·81	20·02	25·76	22·90	18·36	17·16	14·91	18·43	20·84	23·50	27·05	18·50
MgO	45·45	41·85	36·44	39·04	41·81	43·65	45·15	41·89	39·78	37·91	35·59	40·93
MnO	0·20	0·24	0·33	0·23	0·11	0·24	0·17	0·22	0·26	0·33	0·38	0·19
CaO	0·00	0·00	0·00	0·00	0·04	0·01	0·01	0·00	0·00	0·00	0·00	0·02
Na_2O	0·00	0·00	0·10	0·00	0·07	0·06	0·00	0·08	0·00	0·00	0·00	0·03
Cr_2O_3	0·00	0·00	0·00	0·00	0·00	0·00	0·03	0·06	0·00	0·00	0·00	0·04
NiO	0·11	0·19	0·26	0·18	0·14	0·26	0·30	0·22	0·10	0·09	0·07	0·33
ZnO	0·00	0·00	0·00	0·00	0·00	0·00	0·02	0·00	0·00	0·00	0·00	0·00
V_2O_3	0·00	0·00	0·05	0·00	0·00	0·02	0·00	0·00	0·00	0·00	0·00	0·00
Total	99·92	100·11	99·77	100·99	99·828	99·96	99·58	100·31	99·61	99·83	99·19	99·95
Fo%	85	79	72	75	80	82	84	80	77	74	70	80
Sample:	BO1	BO 6	FD1-1	FD1-2	FD4	GV1230	GV1232	GV1262	GV1279	VM1327	VM140B	PC1220A
Rock type:	Px	Gb	Px	Px	Px	Px	Gb-Dior	Px	Px	peg-Gb	Px	Px
Orthopyroxene												
SiO_2	53·95	52·06	50·31	54·05	53·58	53·71	50·46	53·84	55·22	51·60	52·85	51·53
TiO_2	0·10	0·04	1·14	0·04	0·12	0·04	0·04	0·07	0·02	0·10	0·07	0·10
Al_2O_3	2·05	3·32	4·08	2·03	2·32	3·42	2·34	3·41	2·41	3·41	3·45	4·17
FeO	12·26	18·58	15·19	15·59	12·42	11·74	24·96	12·03	12·59	21·07	14·87	12·44
MgO	31·10	24·65	25·87	28·30	30·45	29·89	20·44	29·14	28·42	20·83	0·34	0·26
MnO	0·28	0·36	0·26	0·11	0·30	0·34	0·97	0·28	0·28	0·58	27·08	28·36
CaO	0·16	0·49	1·60	0·15	0·08	0·15	0·43	0·24	0·20	1·57	0·70	0·49
Na_2O	0·09	0·07	0·52	0·06	0·02	0·00	0·08	0·06	0·07	0·32	0·04	0·03
K_2O	0·00	0·00	0·00	0·00	0·00	0·00	0·00	0·00	0·00	0·00	0·01	0·00
Cr_2O_3	0·11	0·00	0·24	0·04	0·00	0·18	0·16	0·13	0·17	0·00	0·07	0·03
NiO	0·09	0·06	0·16	0·08	0·00	0·00	0·01	0·00	0·14	0·13	0·06	0·13
ZnO	0·00	0·13	0·11	0·00	0·32	0·01	0·00	0·00	0·00	0·00	0·00	0·25
V_2O_3	0·00	0·00	0·00	0·00	0·07	0·00	0·00	0·00	0·00	0·12	0·00	0·12
Tot	100·20	99·77	99·48	100·45	99·69	99·49	99·88	99·20	99·54	99·73	99·52	97·90
En%	82	70	73	76	81	82	59	81	80	62	76	80

See Table 1 for abbreviations.

Table 3: Selected microprobe analyses of clinopyroxene and plagioclase

Sample:	BO1	BO1-3	BO6	VM1-1	VM1-2	VM140B	VM1327	PC1220A
Rock type:	Px	Px	Gb	Px	Px	Px	peg-Gb	Px
Clinopyroxene								
SiO_2	51·37	51·85	50·13	50·06	52·06	50·85	51·96	49·60
TiO_2	0·44	0·46	1·07	0·50	0·11	0·88	0·40	0·65
Al_2O_3	3·67	3·56	5·10	10·63	0·89	4·51	4·13	5·91
FeO	3·41	3·34	6·28	6·00	10·69	5·32	7·97	4·31
MnO	0·13	0·17	0·87	0·09	0·33	0·15	0·24	0·13
MgO	16·22	15·83	13·01	18·63	22·01	13·85	13·05	14·65
CaO	23·48	23·40	20·19	10·54	11·19	23·20	20·73	22·30
Na_2O	1·06	0·96	0·61	1·72	0·57	1·02	1·24	0·79
K_2O	0·01	0·00	0·06	0·25	0·00	0·00	0·00	0·01
Cr_2O_3	0·38	0·35	0·34	0·51	0·29	0·27	0·00	0·08
NiO	0·00	0·00	0·05	0·04	0·07	0·01	0·02	0·00
ZnO	0·00	0·00	0·43	0·00	0·00	0·00	0·05	0·06
V_2O_3	0·00	0·35	0·12	0·04	0·00	0·00	0·03	0·00
Total	100·16	100·27	98·24	99·01	98·20	100·07	99·82	98·49

Sample:	BO1	BO6	FD1-1	FD1-2	GV1232	VM1	VM140B	VM1327
Rock type:	Px	Gb	Px	Px	Gb-Dior	Px	Px	peg-Gb
Plagioclase								
SiO_2	50·17	47·81	55·71	52·55	52·61	52·04	50·89	52·26
TiO_2	0·00	0·04	0·05	0·01	0·04	0·03	0·00	0·03
Al_2O_3	31·55	30·71	28·44	31·49	26·97	30·88	29·12	28·21
FeO	0·37	0·00	0·15	0·08	0·08	0·12	0·12	0·32
MnO	0·00	0·00	0·00	0·00	0·00	0·03	0·00	0·02
MgO	0·03	0·04	0·00	0·00	0·00	0·00	0·04	0·04
CaO	14·33	15·86	9·61	12·48	11·59	12·77	12·64	11·96
Na_2O	3·56	4·45	6·02	4·62	8·83	4·78	4·39	8·26
K_2O	0·01	0·00	0·04	0·02	0·21	0·02	0·04	0·01
Total	100·02	98·91	100·00	101·24	100·34	100·66	97·23	101·10
An%	69	66	47	60	42	60	63	44

See Table 1 for abbreviations.

grains reveals a complex pattern of zoning with F-rich cores and increased Cl/F ratio and LREE to the rims. The granular spinel is green, aluminous hercynite with Cr_2O_3 in the range 1·4–17·6 wt %. TiO_2 and V_2O_3 reach maximum concentrations of 0·4 wt % and 0·17 wt %, respectively, whereas the ZnO is remarkably high, varying between 0·53 and 2·96 wt % with increasing Cr content. The spinel from the vermicular symplectites is almost Cr-free hercynite with high Al and Mg. Ilmenite exhibits reciprocal substitution of geikielite and pyrophanite end-members, from MgO ~4·8 wt % and MnO ~0·68 wt % to MgO ~0·05 wt % and MnO ~4·2 wt %. Carbonates associated with phlogopite consist of Fe-rich dolomite, whereas those occurring in hornblendite vary in composition from calcite to Ni-rich ankerite.

WHOLE-ROCK GEOCHEMISTRY

General

The pipes are composed of silica-undersaturated ultramafic rocks and gabbros with elevated concentrations of TiO_2, Na_2O, K_2O, P_2O_5 and, especially, S (Table 7a). MgO is in the 32–20 wt % range in ultramafic rocks, and 18–6 wt % in gabbroic rocks, exhibiting a negative correlation with Al_2O_3, CaO and Na_2O, and a positive

Table 4: Selected microprobe analyses of amphibole and phlogopite

Sample:	BO1	BO6	FD1	FD3	FD4	GV1230	GV1262	GV1279	PC1220	VM1327	VM1	VM140B
Rock type:	Px	Gb	Px	Px	Px	Px	Px	Px	Px	peg-Gb	Px	Px
Amphibole												
SiO_2	41·43	40·96	45·00	42·45	43·81	42·16	42·24	42·14	41·66	40·08	40·93	40·30
TiO_2	3·42	2·69	2·23	0·77	1·27	2·19	2·08	0·55	2·68	2·86	0·46	3·63
Al_2O_3	14·23	15·51	12·13	15·64	15·11	14·61	15·01	15·03	14·66	15·17	17·04	15·58
FeO	6·14	9·91	7·25	6·91	6·19	6·96	7·55	7·36	7·31	12·22	8·07	10·11
MnO	0·06	0·13	0·17	0·17	0·05	0·09	0·12	0·13	0·11	0·14	0·09	0·15
MgO	15·16	12·67	16·66	16·21	17·11	15·54	15·71	15·89	14·02	10·90	14·78	12·01
CaO	11·56	12·23	11·83	12·78	11·46	11·39	11·57	11·39	11·62	10·57	12·31	12·40
Na_2O	3·30	2·37	2·71	2·82	2·88	4·03	3·89	4·85	3·32	5·13	3·10	2·84
K_2O	0·88	1·23	0·41	0·56	0·18	0·44	0·37	0·72	0·36	0·85	1·33	1·68
Cr_2O_3	0·60	0·00	0·24	0·34	0·69	0·42	0·29	0·16	0·28	0·05	0·18	0·02
NiO	0·04	0·01	0·18	0·10	0·04	0·09	0·03	0·17	0·05	0·00	0·00	0·00
ZnO	n.d.	0·50	0·00	0·00	0·00	n.d.	0·11	0·00	n.d.	0·00	0·00	n.d.
V_2O_3	n.d.	0·14	0·16	0·00	0·14	n.d.	0·00	0·03	n.d.	0·12	0·00	n.d.
Total	96·82	98·36	98·97	98·73	98·93	97·91	98·97	98·42	96·07	98·10	98·31	98·74
F	b.d.l.	0·06	0·03	n.d.	n.d.	0·06	0·05	b.d.l.	n.d.	0·25	0·10	0·12
Cl	0·04	0·02	0·04	n.d.	n.d.	0·05	0·02	0·05	n.d.	0·05	0·02	0·03

Sample:	BO1	BO6	FD1	FD4-1	FD4-2	GV1230	GV1232	GV1262	GV1279	VM140B	VM1-1	VM1-2
Rock type:	Px	Gb	Px	Px	Px	Px	Gb-Dior	Px	Px	Px	Px	Px
Phlogopite												
SiO_2	38·62	37·17	39·86	40·18	39·61	38·89	36·29	38·79	37·50	37·68	38·14	35·51
TiO_2	3·93	5·02	1·77	0·80	1·05	3·10	6·45	3·25	3·79	3·10	2·00	3·54
Al_2O_3	16·74	16·96	16·67	17·69	18·31	17·69	15·60	16·99	17·61	17·23	18·14	18·81
FeO	6·63	10·17	6·83	4·31	4·80	5·38	14·02	5·67	6·49	8·18	7·77	7·83
MnO	0·00	0·05	0·00	0·00	0·00	0·04	0·10	0·04	0·04	0·06	0·08	0·01
MgO	20·67	17·33	21·87	24·33	22·96	22·46	14·32	21·89	19·75	20·24	21·53	19·18
CaO	0·00	0·07	0·00	0·02	0·03	0·01	0·09	0·00	0·04	0·06	0·03	0·29
Na_2O	1·06	0·61	1·66	1·48	2·09	1·42	0·05	1·82	1·09	1·01	1·15	0·76
K_2O	8·74	8·19	7·17	6·78	6·15	7·12	8·70	7·82	9·17	8·45	7·20	8·46
Cr_2O_3	0·30	0·26	0·09	0·41	0·61	0·17	0·22	0·31	0·18	0·00	0·34	0·43
NiO	0·08	0·05	0·08	0·10	0·00	0·02	0·09	0·07	0·14	0·03	0·04	0·15
ZnO	0·22	n.d.	n.d.	n.d.	0·09	0·10	0·01	n.d.	0·01	n.d.	n.d.	0·23
V_2O_3	0·14	n.d.	n.d.	n.d.	0·11	0·06	0·08	n.d.	0·09	n.d.	n.d.	0·11
Total	97·14	95·88	96·00	96·09	95·81	96·46	96·01	96·64	95·90	96·03	96·42	95·31
F	0·10	0·33	0·11	0·35	0·22	0·30	0·04	0·21	n.d.	0·16	0·19	0·11
Cl	0·02	0·02	0·02	0·02	0·06	0·02	0·04	0·04	n.d.	0·03	b.d.l.	0·08

n.d., not determined, b.d.l., below detection limit. (See Table 1 for the other abbreviations.)

Table 5: Selected microprobe analyses of spinel and ilmenite

Sample:	BO1	BO6	FD1	FD3	FD4	GV1230	GV1262	GV1279	VM1	PC1220A
Rock type:	Px	Gb	Px	Px	Px	Px	Px	Px	Px	Px
Spinel										
SiO_2	0·02	0·06	0·04	0·15	0·28	0·00	0·14	0·18	0·03	0·00
TiO_2	0·00	0·02	0·11	0·03	0·40	0·02	0·05	0·00	0·03	0·03
Al_2O_3	63·66	52·36	42·29	58·94	51·03	61·67	58·59	63·14	52·65	61·28
FeO	18·65	23·84	26·14	20·56	19·65	15·24	16·20	16·37	20·65	14·99
Fe_2O_3*	2·05	1·15	3·38	0·71	0·09	2·82	3·59	1·11	4·76	2·50
MgO	15·22	9·15	7·61	11·50	11·98	16·52	15·53	16·29	12·54	16·73
MnO	0·06	0·20	0·18	0·29	0·15	0·14	0·12	0·02	0·15	0·12
Cr_2O_3	0·00	9·25	17·61	3·61	12·93	1·93	3·85	1·42	8·31	1·83
NiO	0·00	0·26	0·03	0·04	0·13	0·39	0·27	0·20	0·13	0·29
ZnO	0·00	1·57	3·11	2·96	2·60	0·53	1·03	0·64	1·42	0·56
V_2O_3	0·00	0·06	0·00	0·06	0·17	0·03	0·05	0·18	0·02	0·23
Total	99·66	97·92	100·50	98·85	99·41	99·29	99·42	99·55	100·69	98·56
Sample:	BO1-1	BO1-2	BO6	FD1-1	FD1-2	FD1-3	FD4-1	FD4-2	GV1232	VM1327
Rock type:	Px	Px	Gb	Px	Px	Px	Px	Px	Gb-Dior	peg-Gb
Ilmenite										
SiO_2	0·03	0·02	0·03	0·00	0·03	0·18	0·14	0·09	0·03	0·05
TiO_2	54·71	54·08	51·70	53·24	51·15	51·04	52·21	53·59	48·51	50·54
Al_2O_3	0·12	0·00	0·00	0·07	0·00	0·02	0·00	0·01	0·00	0·00
FeO	38·46	41·01	45·67	44·59	43·84	42·25	41·88	40·33	47·58	45·10
MgO	4·95	4·49	0·24	1·73	0·26	0·06	1·15	4·05	0·67	1·13
MnO	0·69	0·71	1·93	0·82	3·98	4·15	1·10	0·77	1·52	2·49
CaO	0·02	0·08	0·05	0·00	0·01	0·11	0·05	0·01	0·01	0·00
Na_2O	0·13	0·00	0·00	0·04	0·00	0·00	0·03	0·04	0·04	0·22
K_2O	0·00	0·00	0·00	0·00	0·00	0·00	0·00	0·00	0·00	0·00
Cr_2O_3	0·11	0·14	0·04	0·00	0·15	0·10	0·25	0·20	0·19	0·06
NiO	0·00	0·00	0·21	0·00	0·02	0·00	0·00	0·00	0·00	0·06
ZnO	0·03	0·00	0·24	0·25	0·00	0·00	0·09	0·00	0·00	0·03
V_2O_3	0·00	0·00	0·00	0·00	0·00	0·00	0·08	0·05	0·00	0·00
Total	99·25	100·53	100·11	100·74	99·44	97·91	96·98	99·14	98·55	99·68

*Calculated assuming spinel stoichiometry. (See Table 1 for abbreviations.)

Table 6: Selected microprobe analyses of apatite

Sample:	BO1-1	BO1-2	FD1-1	FD1-2	GV1230-2	GV1230-3	VM1-1	VM1-2
Rock type:	Px	Px	Px	Px	Px	Px	Px	Px
SiO_2	0·12	0·13	0·16	0·05	0·10	0·06	0·08	0·05
CaO	55·98	56·49	53·72	55·78	54·92	55·74	55·18	54·08
Na_2O	0·24	0·27	0·08	0·03	0·28	0·26	0·03	0·05
P_2O_5	41·12	40·42	42·44	42·22	41·87	40·75	42·14	42·57
Ce_2O_3	0·11	0·13	0·14	0·21	0·10	0·19	0·04	0·05
La_2O_3	0·04	0·11	0·19	0·11	0·11	0·04	b.d.l.	b.d.l.
Nd_2O_3	0·06	0·27	b.d.l.	0·12	0·00	0·23	0·17	b.d.l.
Pr_2O_3	0·09	0·06	0·00	0·11	0·00	0·21	0·05	0·00
ZrO_2	0·03	0·42	0·23	0·00	0·35	0·00	0·02	0·00
HfO_2	b.d.l.	0·28	0·00	0·00	0·00	0·00	0·43	0·09
Y_2O_3	b.d.l.	b.d.l.	0·00	0·00	0·07	0·00	0·00	0·00
Total	97·79	98·58	96·96	98·63	97·80	97·48	98·14	96·89
Cl	0·51	0·51	0·56	0·33	1·70	1·92	1·64	2·37
F	1·27	1·35	3·84	1·53	0·47	0·75	1·34	0·90

n.d., not determined, b.d.l., below detection limit. (See Table 1 for the other abbreviations.)

correlation with Cr_2O_3. TiO_2 (0·3–3·34 wt %), K_2O (0·07–0·79 wt %), and P_2O_5 (0·06–0·97 wt %) are well correlated but do not show any significant correlation with MgO or any other major oxide. Mid-ocean ridge basalt (N-MORB)-normalized trace-element patterns (Fig. 2) reveal that the pipes are enriched in both incompatible and the most compatible elements but depleted in elements of intermediate compatibility. All pipes have intense positive anomalies in Pb, Cu and Ni, and less intense anomalies in Sr. All but Fei di Doccio also have a positive anomaly in Ba and a less intense (and limited to a few samples) anomaly in Eu. All except Castello di Gavala have a moderate positive anomaly in K. Zr and Hf are strongly enriched in Bec d'Ovaga and, to a lesser extent, in some samples from Valmaggia and Fei di Doccio, but show a considerable depletion in one sample from Castello di Gavala. All pipes have an intense negative Nb anomaly and a less intense Ti one (with the exception of Castello di Gavala).

Large ion lithophile and high field strength elements

Rb (0·6–16 ppm), Cs (0·04–1·2 ppm) and Tl (0·01–0·32 ppm) exhibit a positive correlation with K_2O, except in the most K-rich samples from Bec d'Ovaga, where the correlation becomes negative. Li (0·42–20 ppm) correlates well with Cs and Tl, but not with Rb and K. Remarkably, the highest concentrations of Rb, Cs, Tl and Li occur in the most magnesian samples (Fig. 3a; see also Fig. 8, below). The concentration of Sr is high, varying in the range 69–216 ppm and 351–528 ppm in pyroxenites and gabbros, respectively; it displays an excellent positive correlation with Al, Na, Ca and Ga. Ba varies greatly (20–1396 ppm) and can be unusually high in the ultramafic rocks, showing a positive correlation with Eu, K, P and Zr (Figs 3c and 8, below). Zr is commonly in the range of 50–150 ppm except in the Bec d'Ovaga samples, where it reaches concentrations of >900 ppm.

Nb (0·5–6·3 ppm), Ta (0·05–0·4 ppm) and Be (0·3–0·9 ppm) are excellently correlated with each other and display a good correlation with Y. The Nb/Ta ratio has a nearly constant value of Nb/Ta $\sim$14·6 (Fig. 3d), slightly lower than usual for mantle rocks ($\sim$17·5; Green, 1995), probably reflecting the presence of amphibole in the source. Zr/Nb ratios are extremely variable, and reflect two trends, one with Zr/Nb $\sim$200 for the Bec d'Ovaga and the Zr-richest samples of Valmaggia, and the other with Zr/Nd $\sim$25 for the rest (Fig. 3e). U (0·05–0·8 ppm) and Th (0·2–2·5 ppm) are abnormally elevated for ultramafic rocks and, similarly to Li, Rb, Cs and Tl, they reach their maximum concentration levels in the more magnesian samples (Fig. 3b). Th/U ratios are very close to the mantle value of Th/U = 3·7 (Fig. 3f) (Rogers & Adams, 1969) for all but the Fei di Doccio samples, which are enriched in Th, and one sample from Bec d'Ovaga, which is strongly enriched in U, Ba, Zr, Nb and LREE. Sc (4–25 ppm) and V (50–300 ppm)

Table 7a: Major- and trace-element data for rocks from the Ivrea–Verbano ultramafic pipes

Sample:	BO1	BO6	BO9	BO1250	BO1253	BO1272	FD1	FD2	FD3	FD4	FD6	GV1224	GV1228
Rock type:	Px	Gb	Px	Px	Px	Px	Px	Px	Horn	Px	Px	Gb	Gb
SiO_2	40·55	41·74	40·60	41·18	41·22	39·42	43·14	34·82	27·37	42·37	44·62	43·32	45·87
TiO_2	0·73	1·30	0·68	0·80	1·39	1·62	1·23	0·30	0·40	0·78	0·95	3·34	1·31
Al_2O_3	7·83	17·17	6·65	8·93	7·38	8·83	8·74	4·40	14·11	8·09	8·82	20·12	18·94
Fe_2O_3	15·96	17·31	15·83	14·21	13·34	22·28	16·33	24·93	33·57	14·20	15·52	12·97	12·36
MnO	0·17	0·17	0·17	0·17	0·17	0·23	0·18	0·11	0·12	0·19	0·19	0·16	0·21
MgO	27·47	9·82	29·05	27·50	28·48	20·68	22·92	32·49	17·92	28·75	22·86	5·80	8·74
CaO	5·77	9·92	5·39	5·35	6·04	4·35	5·35	1·98	4·98	3·63	5·70	12·64	10·42
Na_2O	1·15	1·62	0·94	1·43	1·17	0·98	1·42	0·61	1·21	1·27	0·70	1·34	1·49
K_2O	0·24	0·79	0·52	0·23	0·59	0·78	0·44	0·19	0·19	0·49	0·43	0·22	0·33
P_2O_5	0·12	0·17	0·17	0·20	0·20	0·82	0·26	0·16	0·12	0·23	0·21	0·08	0·33
S	1·98	3·76	1·33	0·12	0·19	4·13	1·74	11·40	17·50	1·66	1·34	0·09	0·09
Cu	517	536	4333	52	84	2987	754	744	578	381	81	28	38
Ni	3781	5733	1142	906	107	4475	3099	6043	9299	1578	837	12	98
Co	158	207	85	94	94	161	142	362	553	99	90	38	42
Zn	52	58	62	53	65	242	92	18	1202	100	69	102	98
Mo	1·32	1·43	0·51	0·40	0·54	2·55	1·19	2·24	2·23	0·80	0·70	0·07	0·13
Sn	4·05	0·00	0·00	0·00	0·00	0·08	0·23	7·95	22	0·83	0·00	0·92	0·16
Pb	17	16	9·64	1·84	3·44	39	7·49	19	32	7·39	6·35	4·81	2·93
Cr*	1762	728	2006	2740	2260	1390	800	470	1595	2000	842	13	288
U	0·12	0·14	0·37	0·12	0·32	0·75	0·34	0·26	0·44	0·35	0·35	0·30	0·07
Th	0·42	0·44	1·59	0·42	1·27	0·87	1·59	1·03	2·47	1·74	1·60	0·21	0·25
Be	0·48	0·61	0·52	0·63	0·78	0·76	0·97	0·49	0·83	0·78	0·87	0·38	0·53
Ta	0·16	0·20	0·14	0·21	0·29	0·36	0·39	0·16	0·24	0·32	0·32	0·06	0·15
Nb	2·27	3·19	2·14	2·93	4·42	5·15	6·34	2·39	3·18	4·73	5·04	3·01	2·47
Rb	6·52	9·39	15	5·05	13	11	13	5·39	6·87	16	10	n.d.	2·63
Cs	0·21	0·26	0·89	0·16	0·55	0·37	1·21	0·82	0·38	1·20	0·98	n.d.	0·06
Tl	0·05	0·07	0·17	0·04	0·11	0·15	0·15	0·21	0·90	0·32	0·13	n.d.	0·02
Li	4·19	4·69	3·93	2·32	3·72	6·83	15	9·26	13	19	6·50	0·42	4·00
Sc	18	25	17	17	24	17	20	10	4	13	19	67	54
V	107	182	115	118	205	137	147	64	140	98	115	652	293
Sr	185	379	177	216	183	216	182	122	224	155	175	406	434
Ga	5·71	13	6·14	7·06	9·06	12	11	5·50	19	9·43	9·32	18·62	18·62
Ba	120	659	118	62	244	1396	129	42	34	91	89	290	324
Y	9·82	15	10	11	20	20	21	6·03	6·02	15	18	12	15
Zr*	330	610	225	71	190	905	113	86	37	96	72	27	35
Hf	1·30	1·99	1·16	1·29	2·68	5·73	1·96	0·92	0·93	1·81	2·04	1·04	1·27
La	4·22	6·71	6·61	4·81	8·51	17	11	5·03	9·24	9·46	10	8·87	13
Ce	11	16	16	12	22	40	27	11	18	23	24	18	29
Pr	1·54	2·37	2·33	1·75	3·47	5·45	3·85	1·38	2·36	3·17	3·39	2·82	4·11
Nd	7·02	11	11	7·96	17	24	17	5·63	9·45	13	15	12	19
Sm	1·80	2·73	2·62	1·98	4·27	4·84	4·12	1·17	1·80	3·00	3·57	2·85	3·61
Eu	0·64	1·43	0·77	0·69	1·35	3·10	1·16	0·35	0·50	0·83	0·97	1·59	2·07
Gd	1·82	2·53	2·19	2·07	3·95	4·25	3·69	1·05	1·45	2·72	3·28	2·44	3·27
Tb	0·28	0·40	0·33	0·34	0·58	0·58	0·59	0·16	0·22	0·43	0·52	0·38	0·45
Dy	1·81	2·73	1·84	2·05	3·61	3·49	3·92	1·10	1·28	2·79	3·32	2·21	2·74
Ho	0·37	0·57	0·38	0·43	0·74	0·72	0·79	0·23	0·25	0·56	0·67	0·46	0·56
Er	0·96	1·47	0·96	1·14	1·95	1·94	2·04	0·65	0·66	1·48	1·82	1·24	1·44
Tm	0·14	0·22	0·14	0·16	0·28	0·29	0·31	0·10	0·09	0·22	0·27	0·18	0·21
Yb	0·79	1·22	0·76	0·88	1·52	1·72	1·72	0·56	0·52	1·31	1·56	1·12	1·14
Lu	0·12	0·18	0·11	0·14	0·23	0·27	0·25	0·08	0·08	0·20	0·23	0·16	0·18

Table 7b: Major and trace element data for rocks from the Ivrea-Verbano ultramafic pipes

Sample	GV1230	GV1232	GV1235	GV1262	GV1279	VM1	VM3	VM140B	VM1326	VM1327	VM1328	VM1329	PC1220A
Rock type:	Px	Gb-Dior	Gb	Px	Px	Px	Px	Px	Px	peg-Gb	peg-Gb	Px	Px
SiO_2	42·45	38·71	46·42	41·46	37·08	39·29	37·55	39·21	38·43	37·90	45·08	40·45	41·64
TiO_2	0·87	1·01	0·60	0·86	0·68	0·49	0·41	0·56	0·74	2·02	0·69	0·66	0·69
Al_2O_3	7·92	21·00	22·49	7·83	7·10	5·59	5·14	8·50	5·36	12·22	19·76	4·01	8·13
Fe_2O_3	13·86	23·86	7·95	14·25	21·34	20·66	21·69	19·73	26·06	27·13	11·49	21·40	15·24
MnO	0·17	0·09	0·15	0·15	0·16	0·22	0·23	0·21	0·24	0·20	0·09	0·23	0·19
MgO	27·72	2·82	6·94	28·47	27·54	28·70	28·88	25·50	24·88	8·13	7·55	25·78	23·22
CaO	5·26	8·09	13·56	5·23	4·89	4·05	4·67	5·19	3·43	10·44	12·68	7·12	9·80
Na_2O	1·25	3·07	1·51	1·24	0·79	0·73	0·73	0·82	0·40	1·73	2·18	0·21	0·95
K_2O	0·28	0·38	0·27	0·30	0·28	0·17	0·70	0·20	0·29	0·15	0·30	0·08	0·07
P_2O_5	0·21	0·97	0·10	0·21	0·14	0·10	n.d.	0·08	0·16	0·08	0·19	0·06	0·08
S	0·99	13·70	0·08	1·53	8·30	3·39	2·89	2·05	1·88	0·85	2·33	1·61	2·71
Cu	1259	9126	22	1921	9858	1182	1031	1804	1086	893	2190	790	1078
Ni	2291	13040	39	2737	7525	2724	2587	1917	3415	2750	2361	1964	4334
Co	100	350	30	116	234	213	194	164	259	202	132	165	154
Zn	68	58	35	67	135	103	77	93	54	102	36	55	68
Mo	2·02	3·04	0·08	1·03	1·63	0·65	0·43	0·55	0·80	0·43	0·48	0·25	1·17
Sn	1·66	2·16	0·88	3·47	2·40	3·75	1·06	0·00	0·83	1·13	0·76	0·58	1·40
Pb	51	51	2·02	30	21	2·88	2·76	5·08	3·20	7·98	6·17	3·61	7·13
Cr*	1352	291	200	1680	1170	840	2200	2231	765	68	207	1386	1250
U	0·29	0·10	0·32	0·26	0·12	0·10	0·32	0·06	0·13	0·08	0·13	0·10	0·04
Th	1·10	0·26	0·22	1·04	0·52	0·28	0·13	0·18	0·42	0·25	0·42	0·18	0·16
Be	0·70	0·35	0·37	0·70	0·45	0·55	0·22	0·33	0·55	0·42	0·68	0·30	0·43
Ta	0·20	0·10	n.d.	0·21	0·14	0·11	n.d.	0·07	0·25	0·11	0·18	0·10	0·09
Nb	3·00	1·88	0·88	2·99	2·03	1·41	n.d.	0·81	4·02	1·52	2·96	0·54	1·25
Rb	6·70	6·03	n.d.	9·11	7·35	2·63	n.d.	3·33	6·49	2·49	5·40	1·68	0·60
Cs	0·62	0·04	n.d.	0·38	0·31	0·19	n.d.	0·12	0·13	0·23	0·29	0·07	0·07
Tl	0·16	0·12	n.d.	0·15	0·15	0·03	n.d.	0·02	0·05	0·10	0·05	0·01	0·02
Li	4·60	3·68	n.d.	3·68	4·01	4·99	1·36	4·58	4·80	7·36	4·46	6·46	2·76
Sc	18	5·16	53	18	15	16	19	12	14	44	28	40	36
V	120	80	147	122	113	88	142	121	91	861	125	142	198
Sr	202	452	518	206	151	127	120	213	108	351	528	69	69
Ga	7·89	14	17	7·86	5·61	5·50	4·68	7·12	5·81	18	15	5·00	7·76
Ba	74	758	426	72	185	145	24	219	127	84	173	104	20
Y	13	6·62	12	13	9·24	8·35	5·90	4·58	15	13	17	14	13
Zr*	82	12	75	72	63	82	23	65	67	37	66	58	43
Hf	1·61	0·09	1·74	1·43	1·35	1·27	0·51	1·20	1·75	1·14	1·77	1·53	1·07
La	7·26	24	12	6·71	5·17	3·50	1·63	3·33	5·80	3·26	7·17	2·34	2·13
Ce	17	47	24	16	12	8·51	3·47	7·39	16	8·77	18	7·01	5·98
Pr	2·26	5·71	3·31	2·17	1·58	1·28	0·92	1·00	2·41	1·39	2·63	1·23	1·00
Nd	9·91	24	15	9·41	7·09	5·56	3·49	4·48	11	6·96	12	6·90	5·15
Sm	2·28	3·19	2·98	2·26	1·69	1·41	1·15	0·91	2·80	2·05	3·10	2·22	1·62
Eu	0·76	3·23	1·90	0·72	0·67	0·53	0·33	0·57	0·79	0·79	1·14	0·78	0·56
Gd	2·33	2·73	2·69	2·16	1·66	1·41	0·96	0·90	2·76	2·27	3·11	2·48	1·97
Tb	0·36	0·31	0·40	0·34	0·27	0·22	0·16	0·13	0·43	0·38	0·49	0·40	0·33
Dy	2·33	1·27	2·16	2·20	1·70	1·45	1·06	0·80	2·52	2·32	2·98	2·49	2·29
Ho	0·47	0·24	0·45	0·46	0·36	0·30	0·20	0·17	0·54	0·49	0·64	0·53	0·49
Er	1·30	0·55	1·18	1·22	0·95	0·84	0·60	0·44	1·46	1·29	1·72	1·46	1·33
Tm	0·18	0·07	0·17	0·18	0·13	0·13	0·08	0·06	0·22	0·19	0·25	0·21	0·20
Yb	1·04	0·42	1·08	1·04	0·75	0·75	0·49	0·37	1·37	1·16	1·47	1·26	1·20
Lu	0·16	0·05	0·17	0·16	0·11	0·11	0·08	0·06	0·20	0·17	0·21	0·18	0·17

Major elements have been normalized to 100·00 not including S and LOI. n.d., not determined. *Analysed by XRF.

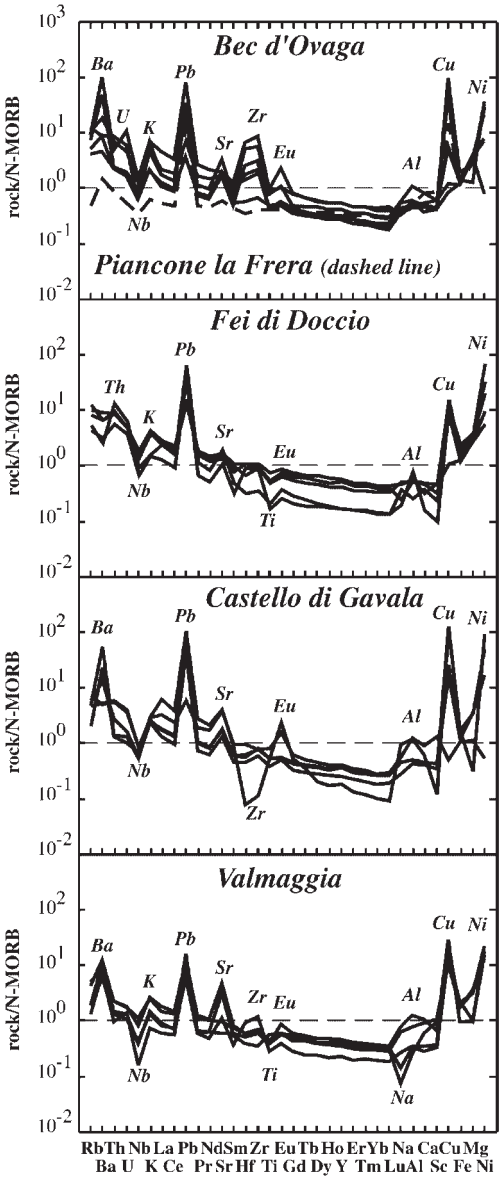

Fig. 2. N-MORB normalized trace-element patterns for the ultramafic pipes [normalization values taken from Hofmann (1988)]. (Note the positive anomalies for all pipes in Pb, Cu, Ni and Sr, and negative anomaly in Nb. See text for details.)

are correlated with each other and also show a weak correlation with Si, Ca, Sr and Ti.

Rare earth elements

The REE contents are also elevated, usually around (20–50) × chondrite for LREE and (5–10) × chondrite for heavy REE (HREE), with LREE/HREE usually in the range of 3–8, except for Piancone la Frera, which has values of about 10 × chondrite for all the REE (Fig. 4). The LREE have an excellent positive correlation with P, as exemplified by the La–P_2O_5 relationships (Figs 5a and 8, below), suggesting major apatite control (neither monazite nor xenotime has been found under the scanning electron microscope). The HREE are better correlated with TiO_2 (Figs 5b and 8, below), probably because of their incorporation in Ti-rich amphibole. The intensity of the europium anomaly is usually close to Eu/Eu* ~1 except in plagioclase-rich samples, where it may be as high as Eu/Eu* ~3. The anomaly has a positive correlation with plagioclase-compatible elements, as shown by its correlation with Sr (Figs 5c and 8, below). However, for Bec d'Ovaga and Castello di Gavala, the anomaly also correlates positively with Ba, Zr and P (Fig. 5d), suggesting the action of metasomatic fluids enriched in Eu.

Sulphur and chalcophile and siderophile elements

The S content of rocks with disseminated sulphides is usually in the range of 1–6 wt %, but may occasionally be either very high (>10 wt %) in samples strongly enriched in secondary sulphide veins, or as low as 0·08 wt % in the weakly disseminated ones. Ni and Cu contents are very high and can reach the per cent level. These two elements, together with the other chalcophile metals Co, Zn, Mo, Pb and Sn, correlate positively with S, thus indicating control by the sulphide phase. The degree of correlation is good (r >0·75) for the pairs Ni–S, Co–S, Ni–Co, Ni–Mo, Mo–Pb, Co–Sn and Sn–Zn, but it decreases notably (r <0·65) for Cu (Fig. 6), as a result of extreme variations in chalcopyrite modal abundance (Garuti *et al.*, 1990). As a consequence of the irregular distribution of chalcopyrite in the sulphide ore of the pipes, Cu/(Cu + Ni) also varies widely from 0·05 to 0·80. However, in the less remobilized nodular ores, the Cu/(Cu + Ni) ratio is more homogeneous, showing progressive Cu enrichment from 0·18 at Fei di Doccio, to 0·34 at Valmaggia, 0·44 at Bec d'Ovaga and 0·52 at Castello di Gavala (Table 8). The bulk average Cu/(Cu + Ni) ratio is ~0·42, much higher than expected for sulphides in ultramafic rocks (Naldrett, 1989) and N-MORB (Hofmann, 1988).

Gold and platinum-group elements

The pipes are the most PGE- and Au-rich sulphide deposits in the Ivrea Zone, containing up to >5 ppm (Pt + Pd) and >20 ppm Au in the bulk sulphide (Table 8). These metals are strictly correlated with the sulphide phase, occurring as discrete mineral inclusions of Pt–Pd tellurides, and Au alloys in the main sulphides, pyrrhotite, pentlandite and chalcopyrite (Garuti & Rinaldi, 1986).

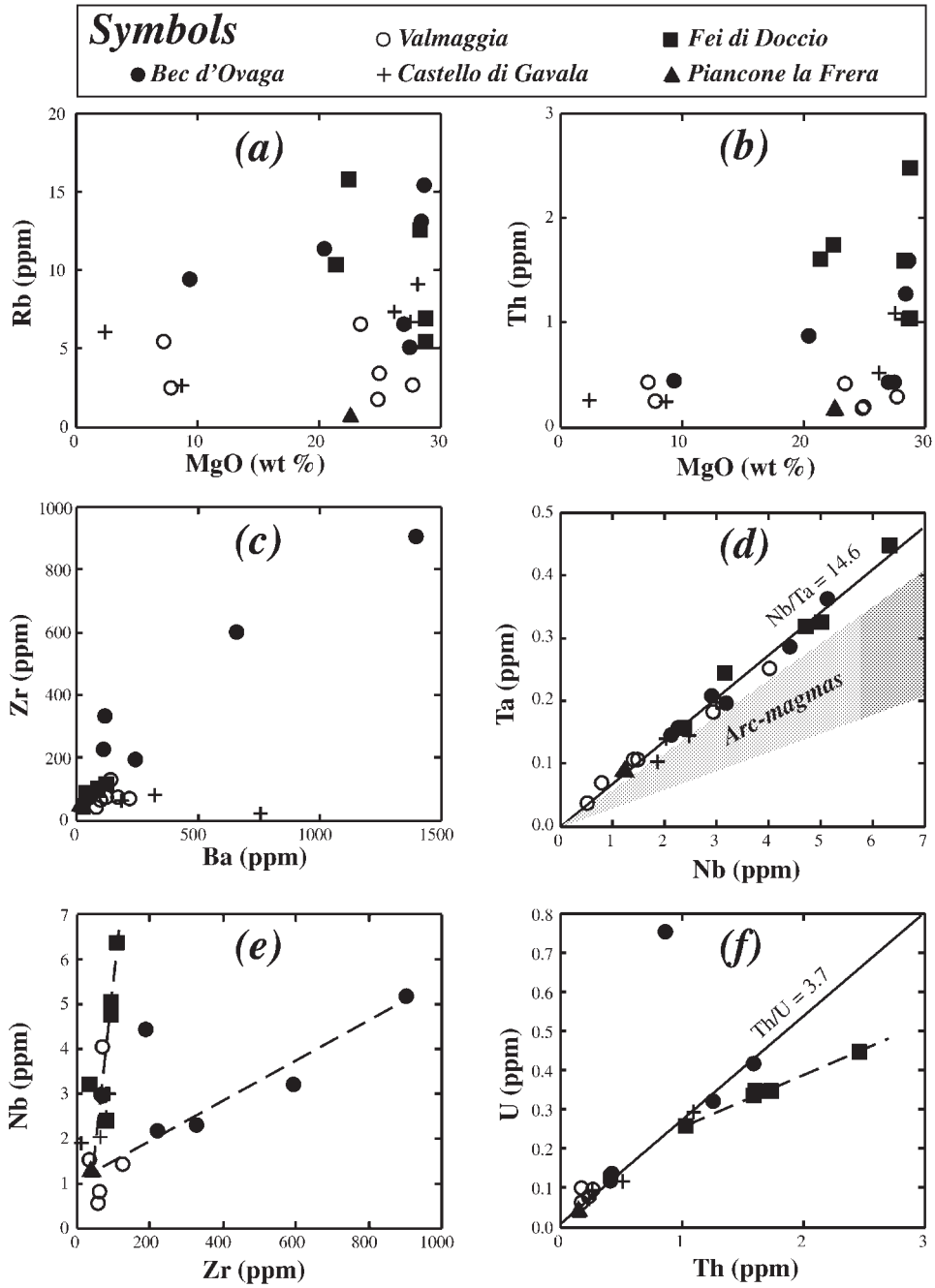

Fig. 3. Selected trace-element variations from the Ivrea Zone ultramafic pipes. The occurrence of the highest concentrations of Rb and Th in the most MgO-rich samples (a) and (b) should be noted, as should the positive correlation between Zr and Ba (c) and the existence of two trends in Nb vs Zr (e) (see text). The shaded area in (d) corresponds to the range of Nb/Ta in arc magmas determined by Stolz *et al.* (1996).

The bulk sulphide, none the less, may contain several hundred ppb of Ir + Os + Ru + Rh, which are not accounted for by any specific phase, and therefore may be present in the sulphides either as a solid solution or as inclusions of submicroscopic metallic clusters (Tredoux *et al.*, 1995). Chondrite-normalized PGE–Au patterns have a fairly positive slope, being notably flatter than the PGE patterns of the other sulphide deposits in the Ivrea

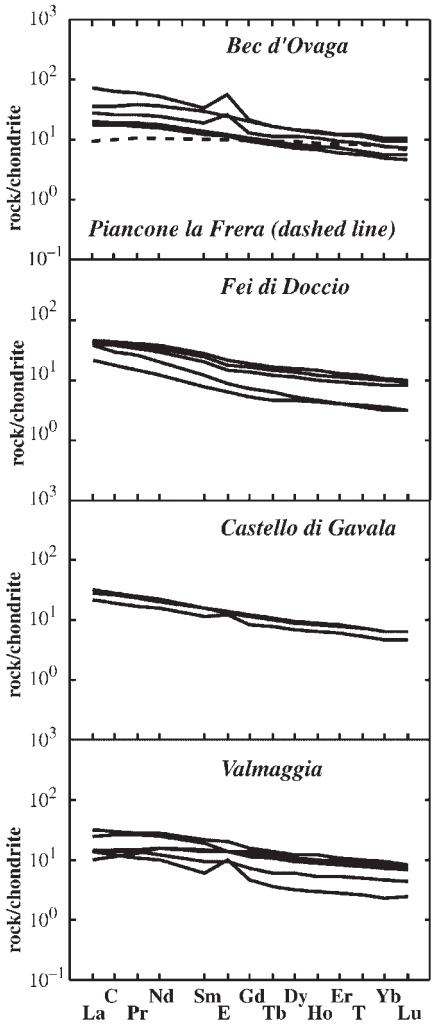

Fig. 4. Whole-rock chondrite-normalized REE patterns for the ultramafic pipes. Normalization values taken from McDonough & Sun (1995).

Zone (Garuti *et al.*, 1990), so that they resemble those of sulphide ores related to komatiites (Fig. 7). The (Pt + Pd)/(Ru + Os + Ir) ratio is in the range 1·12–8·67 (Table 8), consistent with a high-Mg composition for the parent magma (Naldrett, 1989).

Geochemical relationships

Owing to the complex interrelationships among all analysed chemical elements, and to determine whether or not they form groups with a similar behaviour, we have performed a cluster analysis (see Le Maitre, 1982, p. 163) on the dataset formed by all analysed major and trace elements plus two chemical parameters: Eu/Eu* (= $Eu_N/\sqrt{[Sm_N Gd_N]}$), and FeO* (= [Fe^{total} − $Fe^{sulphide}$] expressed as ferrous oxide). As a similarity measure among the variables we have chosen the Pearson correlation coefficient; for amalgamating the variables into hierarchical clusters, we have chosen the complete linkage method, which maximizes the distance between the farthest objects of each cluster (Systat, 1992). The cutoff point to determinate the number of 'natural' clusters was chosen in the first break observed in the variation of the clustering distance with the number of clusters (see the small plot beneath the dendrogram in Fig. 8). This method has produced the following seven groups of highly intercorrelated variables (Fig. 8):

(1) Nb, Ta, Th, U, Be, Li, Rb, Cs and Tl;
(2) MgO, FeO*, MnO and Cr;
(3) S and the chalcophile elements, Cu, Mo, Pb, Ni, Zn, Sn and Co;
(4) Al_2O_3, Na_2O, Ga, Sr and Eu/Eu*;
(5) K_2O, P_2O_5, Ba, LREE, Eu and Zr;
(6) SiO_2, CaO, Sc and V;
(7) TiO_2, MREE, HREE and Y.

The geochemical relationships revealed by cluster analysis can be understood, at least tentatively, in terms of the sequence of crystallization inferred from the textures of the pipes. The presence of skeletal olivine crystals, suggesting rapid growth and partial resorption, and the high magmatic sulphide contents indicate that the magma started to crystallize at depth during its ascent to the lower crust, carrying olivine and immiscible sulphide droplets in suspension at the time of its intrusion. The local enrichment of the magma in early crystals of olivine and Cr-spinel would have produced cluster (2) (Mg, Fe, Mn and Cr). Further crystallization caused the appearance first of clinopyroxene and then of Ti-rich amphibole, whose differential enrichment in definite domains can explain the tendencies expressed by clusters (6) (Si, Ca, Sc and V) and (7) (Ti, MREE and HREE), respectively. The crystallization of amphibole would also have caused some decoupling of Eu^{2+} with respect to Sm^{3+} and Gd^{3+}. As the crystallization of silicates continued, the liquid-sulphide droplets were collected in interstitial spaces, giving rise to local enrichments in sulphides [cluster (3)]. During the last stages of crystallization, small amounts of a differentiated and water-rich silicate liquid, enriched in incompatible elements, was segregated and, depending upon its composition, formed either pods of plagioclase-rich facies with positive Eu anomalies [cluster (4)] such as in Bec d'Ovaga or Castello di Gavala, or local domains rich in phlogopite, plagioclase, apatite, zircon, barite, and carbonates [cluster (5)], enriched in LREE and Eu, but with no Eu anomaly, because the effect of plagioclase (Eu/Eu* >1) was compensated by the effect of apatite (Eu/Eu* <1), such as in Fei di Doccio. The residual hydrothermal fluids remaining after the silicate crystallization, strongly enriched in the most incompatible elements, would finally have caused local metasomatism and enrichment in the

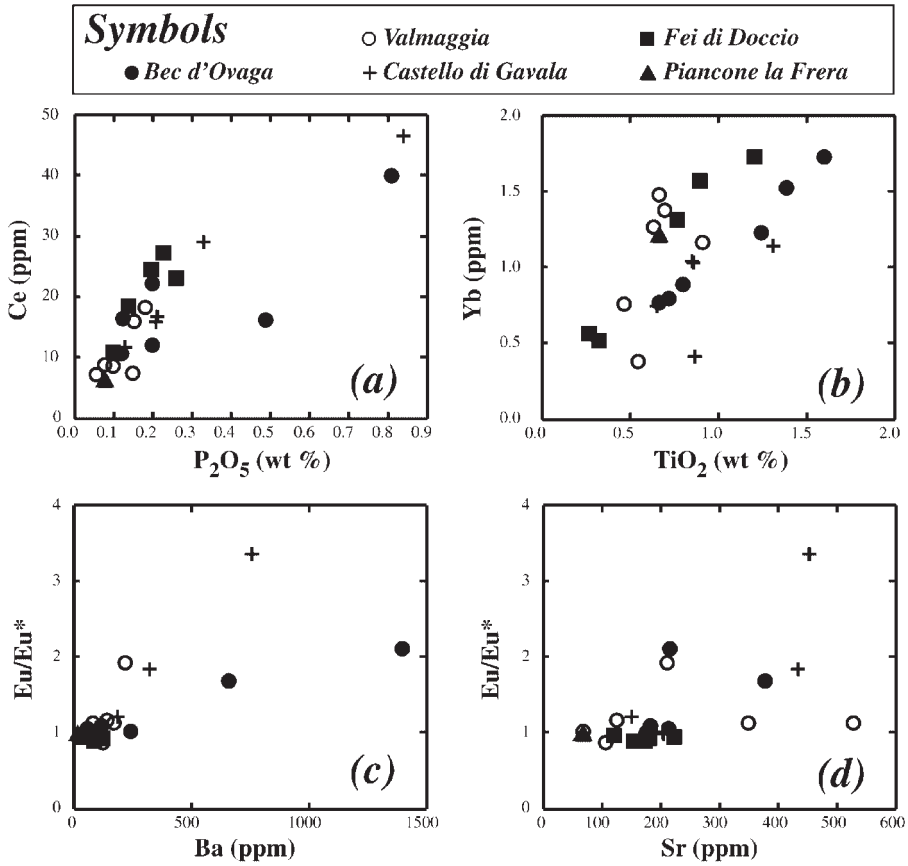

Fig. 5. Whole-rock correlation plots of Ce–P_2O_5 (a) and Yb–TiO_2 (b) indicating the control of apatite and titaniferous hydrous silicates (amphibole, phlogopite) on LREE and HREE, respectively. The correlation between the Eu anomaly and Ba (c) or Sr (d) should be noted. $Eu^* = Eu_N/\sqrt{(Sm_N Gd_N)}$. (See text for explanation.)

Table 8: PGE and Au (ppb) concentrations and relevant metal ratios (by weight) in the sulphide ore of the pipes*

	BO	FD	GV	VM	PC
Os	54–131	42	9–140	9–12	88
Ir	54–108	26–34	12–109	10–14	96
Ru	77–278	24	70–196	85–2949	85
Rh	37–156	12	45–65	5–617	6–56
Pt	375–1114	131	312–3264	50–6569	28–343
Pd	709–1605	228	218–1200	104–2268	7–71
Au	89–1057	145–761	161–23282	18–534	14–915
Pd/Ir	21·75	7·35	27·88	13·74	0·08
Pt/(Pt+Pd)	0·30	0·36	0·61	0·46	0·98
(Pt+Pd)/(Ru+Os+Ir)	8·67	3·70	6·32	6·27	1·12
Cu/(Cu+Ni)	0·44	0·18	0·52	0·34	0·21

*Data from Garuti *et al.* (1990).

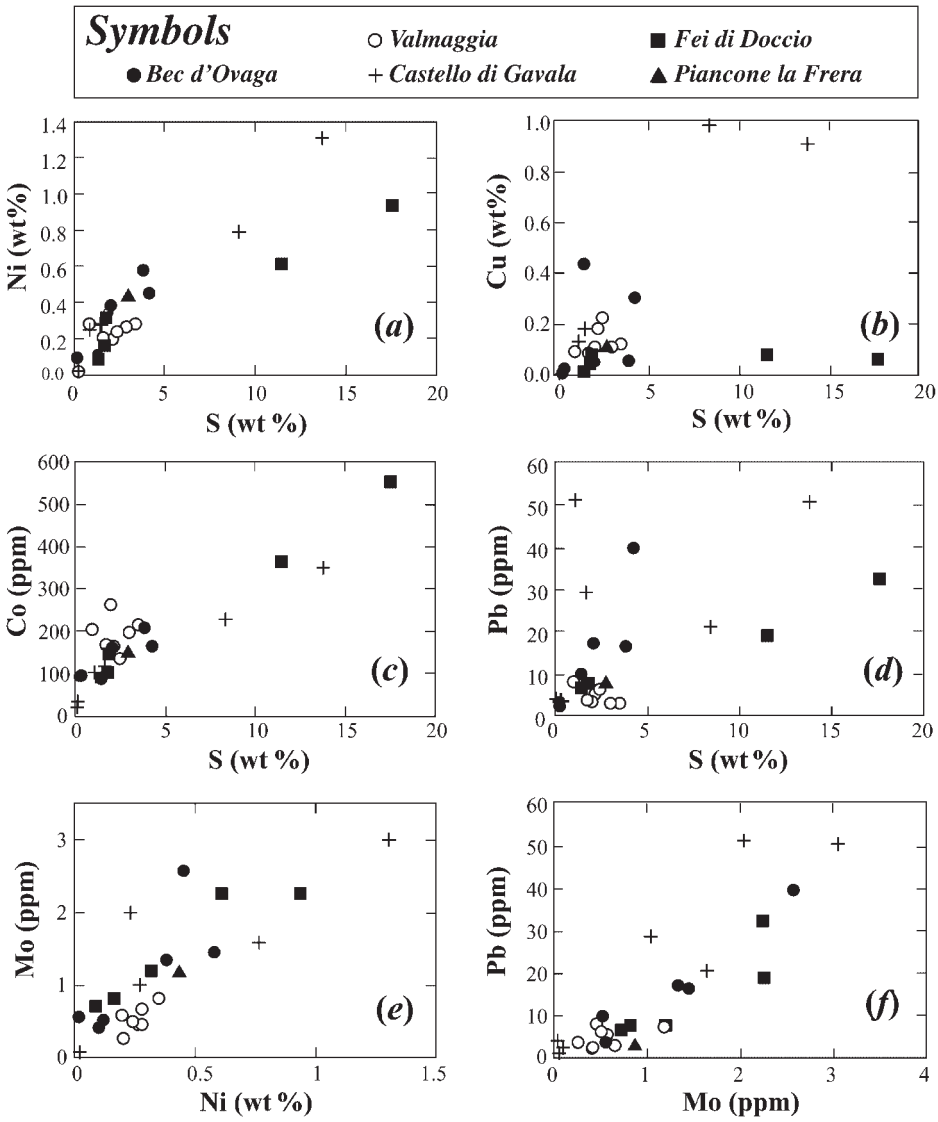

Fig. 6. Whole-rock correlation plots for selected chalcophile elements hosted in the sulphide component of the ultramafic pipes.

elements grouped in cluster (1). This picture, although crude, is indicative of discrete batches of highly mobile magma that suffered strong fractionation on a mesoscopic scale.

CHRONOLOGY AND ISOTOPE GEOLOGY

Zircon ages

The abundance of zircon in some samples from two pipes, Bec d'Ovaga and Fei di Doccio, enabled us to obtain zircon concentrates by conventional heavy-liquid and magnetic separation. Cathodoluminescence scanning electron microscope imaging revealed an internal morphology characteristic of zircons precipitated from a melt, with no inherited cores, oscillatory zoning and, in some cases, kidney-shaped microcrystalline inclusions of silicates that seem to represent pockets of melt trapped during zircon growth. Under the optical and cathodoluminescence–optical microscope, we selected seven zircon grains from a sample from Bec d'Ovaga and five grains from another sample from Fei di Doccio (Table 11, below), ranging in size from 200 mm × 100 mm to 350 mm × 200 mm. They were transparent, colourless or light yellow, prismatic crystals with short and poorly developed pyramids, with no visible fractures or inclusions. Three of the zircons from Bec d'Ovaga were large enough to allow more than one evaporation

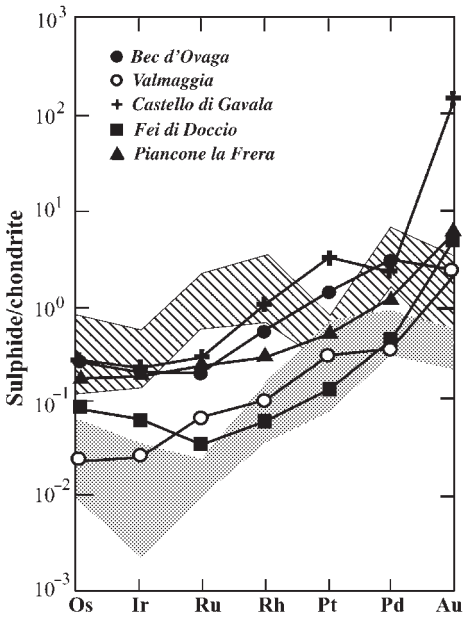

Fig. 7. Chondrite-normalized PGE–Au patterns for pure sulphide from the ultramafic pipes [data from Garuti *et al.* (1990)]. Normalization values are taken from Naldrett (1989). The fields for sulphide deposits in the Ivrea Zone (striped, Garuti *et al.*, 1990), and in komatiites (dark grey, Naldrett, 1989) are shown for comparison.

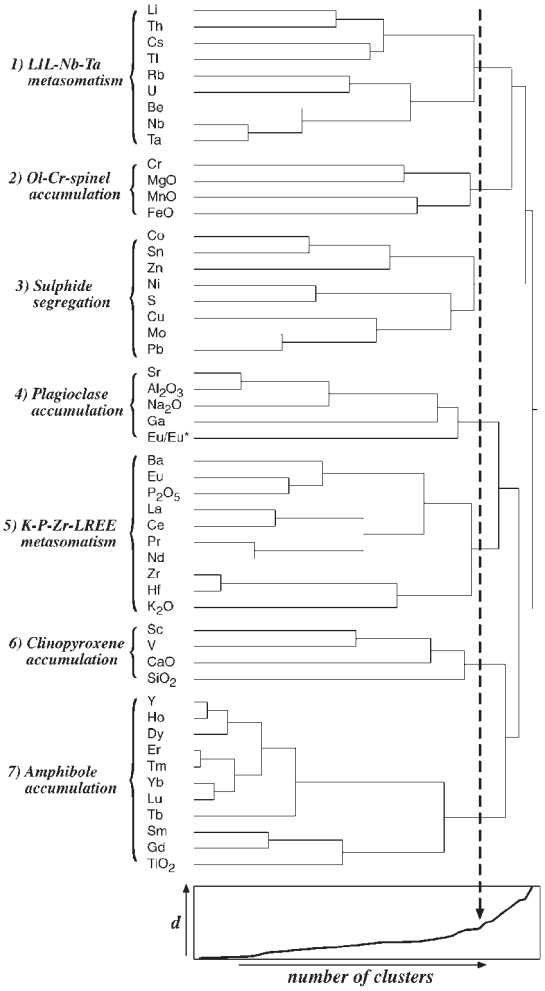

Fig. 8. Cluster-tree showing the interrelations among whole-rock major and trace elements of the pipes. The similarity index is the Pearson correlation coefficient; for amalgamating the variables we have used the complete linkage method, but the single linkage, average, centroid or Ward's methods (Systat, 1992) give nearly the same results. The cutoff point to determine the number of 'natural' clusters was chosen in the first break observed in the variation of the clustering distance *d* with the number of clusters (small plot beneath the dendrogram).

step, in all cases yielding uniform ages. In total we carried out 16 complete evaporation–acquisition cycles that gave average ages of 288 $\pm$ 3 Ma and 287 $\pm$ 3 Ma for Bec d'Ovaga and Fei di Doccio, respectively. Given the internal morphology of zircons, we conclude that these values represent the crystallization age of the pipes. We studied four zircon grains from a sample from the Diorites near Bec d'Ovaga with the same method, obtaining an age of 292 $\pm$ 4 Ma, nearly the same as the pipes. These data are in excellent agreement with the previous U–Pb dating of the Diorites at 285 +7/–5 Ma by Pin (1986) and reveal that the pipes were emplaced shortly after the last massive magmas of the Basic Complex.

Strontium and neodymium isotopes

The $\varepsilon_{290\,Ma}$(Nd) ranges from $-1{\cdot}9$ to $3{\cdot}7$, and the $\varepsilon_{290\,Ma}$(Sr) ranges from 0·8 to 26 (Table 9). In the ε_t(Nd) vs ε_t(Sr) diagram (Fig. 9), the pipes define a curved array towards the lower right part of the diagram, which, remarkably, is placed between the unmetasomatized amphibole peridotites (upper left) and the metasomatized phlogopite peridotites (lower right) of Finero, such that there seems to be a continuous trend formed first by the amphibole peridotites, then by the pipes, and last by the phlogopite peridotites, which, as discussed below, may indicate a genetic relationship between these materials.

Sulphur isotopes

The isotopic composition of sulphur analysed in 14 samples of sulphide concentrates (pyrrhotite + pentlandite + chalcopyrite, Table 10) gave values of $\delta^{34}S$ between 0·0 and +0·9‰, characteristic of mantle sulphides, for all pipes except Fei di Doccio, the one intruded into metasediments. In this case, the $\delta^{34}S$ is higher, $\delta^{34}S \sim +2{\cdot}1$‰, reaching values of $\delta^{34}S = +10{\cdot}1$‰ in samples from the contact with the metapelite (sample FD5, Table 10), thus suggesting a possible introduction

Table 9: Sr and Nd isotope composition of selected samples of the ultramafic pipes

Sample	Rb (ppm)	Sr (ppm)	$^{87}Rb/^{86}Sr$	$^{87}Sr/^{86}Sr$	$\varepsilon_{290\,Ma}(Sr)$	Sm (ppm)	Nd (ppm)	$^{147}Sm/^{144}Nd$	$^{143}Nd/^{144}Nd$	$\varepsilon_{290\,Ma}(Nd)$
GV-1230	6·70	203·0	0·0960	0·704616	0·81	2·30	9·68	0·1435	0·512619	1·60
GV-1232	6·03	452·7	0·0386	0·704432	1·55	3·19	23·56	0·0818	0·512609	3·69
BO-9	15·95	177·8	0·2610	0·706240	14·20	2·61	10·77	0·1466	0·512541	−0·04
BO-6	9·39	380·12	0·0717	0·706322	26·46	2·73	10·88	0·1518	0·512473	−1·56
PC-1220a	0·48	69·4	0·0202	0·704730	6·86	1·68	5·16	0·1965	0·512709	1·40
FD-1	12·55	181·9	0·2006	0·706154	16·52	4·11	16·91	0·1470	0·512472	−1·40
FD-3	6·87	225·0	0·0887	0·705293	10·85	1·80	9·45	0·1152	0·512467	−0·32
VM-1328	5·40	528·9	0·0296	0·705636	19·18	3·11	12·35	0·1522	0·512511	−0·83
VM-1327	2·49	351·9	0·0205	0·705531	18·22	2·05	6·96	0·1779	0·512506	−1·88

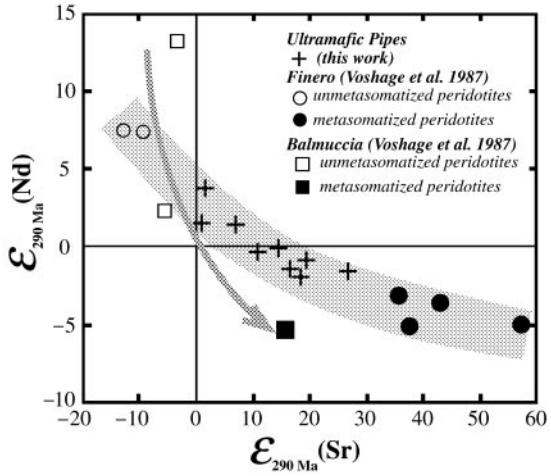

Fig. 9. Variation of $\varepsilon_{290\,Ma}$(Nd) vs $\varepsilon_{290\,Ma}$(Sr) for selected samples of the ultramafic pipes. It should be noted how they form a continuous trend (shaded area) between the unmetasomatized and metasomatized peridotites of Finero, but are oblique with respect to the trend (arrow) defined by the amphibole- and phlogopite-bearing peridotites of Balmuccia [all peridotite data from Voshage *et al.* (1987)].

of sulphur from the surrounding metasediments (Garuti *et al.*, 1986).

DISCUSSION

Nature and origin of pipe magmas

All pipes, irrespective of whether the host rocks are gabbros or metasediments, have similar ultramafic lithologies with textures of indisputable igneous origin. This fact precludes a metasomatic origin, as the metasomatism upon such diverse protholiths would hardly have produced nearly identical rocks. The evidence gathered so far confirms that the ultramafic pipes of the Ivrea Zone derived from limited fractionation and differentiation of high-Mg magmas with alkaline affinities enriched in volatile and incompatible elements (Ferrario *et al.*, 1982; Garuti *et al.*, 1986, 1990).

The isotopic composition of Sr, Nd and S, as well as the geological position of the pipes precludes the high concentrations of incompatible elements being caused by crustal contamination during the ascent of the pipe magma. This feature has been interpreted as a proof of contamination with metasediments [e.g. Sinigoi *et al.* (1994) and references therein], owing to the fact that, in some cases, the leucosomes of the Kinzigite Formation may have positive Eu anomalies. However, the importance of such leucosomes as a potential source for causing the appearance of a positive Eu anomaly in basic magmas through contamination seems to have been overestimated. A systematic study along the Vallestrona d'Omegna section (Bea & Montero, 1999) has revealed

Table 10: Sulphur isotope composition of sulphide concentrates

Sample	Rock type	Total S %	Sulphide ore		$\delta^{34}S$
			type	assemblage	
BO6	Gb	3·76	nodular	po–pn–cp	+0·04
BO9	Px	1·33	nodular	po–pn–cp–py	+0·40
FD1	Px	1·74	nodular	po–pn–cp–mb	+0·80
FD3	Horn	17·5	veins	po–pn–cp–py	+2·10
FD4	Px	1·66	nodular	po–pn–cp	+2·10
FD5	Mp	n.d.	minute layers	po–py	+10·10
GV1230-I	Px	0·99	nodular	po–pn–cp	+0·20
GV1230-II	Px	0·99	nodular	po–pn–cp	+0·30
GV1232-I	Gb–Dior	13·7	veins	cp–po–pn–py	+0·40
GV1232-II	Gb–Dior	13·7	veins	cp–py–po	+0·30
PC1220A-I	Px	2·71	nodular	po–pn–cp–py	0·00
PC1220A-II	Px	2·71	vein	po–py	+0·80
VM1	Px	3·39	nodular	po–pn–cp–mk–cu	+0·30
VM140B	Px	2·05	nodular	po–pn–cp–mk	+0·90

po, pyrrhotite; pn, pentlandite; cp, chalcopyrite; py, pyrite; mb, molybdenite; cu, cubanite; mk, mackinawite. Other abbreviations as in Table 1.

that only the lowest-melt fraction leucosomes, i.e. those segregated within the amphibolite facies, have Eu/Eu* >1, a feature that is always accompanied by very low ΣREE and extremely high SiO_2 contents, and is caused by the preferential incorporation of feldspar to the segregate and the retention of monazite in the residuum (e.g. Bea, 1996). These leucosomes are intimately intermingled with still fertile mesosomes that have Eu/Eu* <1. As the melt fraction increases, the concentration of REE in leucosomes also increases and the Eu anomaly becomes negative. This is the case for all the leucosomes segregated within the granulite facies, which apart from being much more abundant and voluminous, are closer to the Basic Complex and are, thus, the favourite candidates for assimilation. We therefore assume that the elevated concentrations of volatiles and incompatible elements of the pipes probably represent primary features linked either to the nature of the source or to the process of partial melting, or to both.

The interpretation of the trace-element composition of the pipes leads, in principle, to somewhat paradoxical interpretations. On one hand, the high concentrations of volatiles and incompatible elements, together with high Au and Cu and elevated Cu/(Cu + Ni), indicate low degrees of partial melting of a fertile protolith. On the other hand, the elevated concentrations of the most compatible elements, such as Mg and Ni, together with the low (Pt + Pd)/(Ru + Os + Ir), suggest high degrees of melting of a previously depleted source. A possible scenario consists of a depleted mantle protolith flushed with water-rich fluids, either melts or hydrothermal solutions, that had elevated contents of alkalis, alkaline-earths, LREE, Pb, Cu, S, etc. The lowering of the peridotite solidus as a consequence of the increased activity of water (e.g. Wyllie, 1995) caused the harzburgite in the zone percolated by the fluids to undergo partial melting. This mechanism would have produced small pockets of volatile-rich ultramafic magma that evolved as independent intrusions to give rise to the pipes. This is consistent with the fact that all the pipes share many geochemical features reflecting the mixing of two components, although every intrusion still preserves its own particularities (see Figs 2–5).

The pipes were intruded into magmatic and high-grade metamorphic rocks, possibly not much above the crust–mantle transition. This circumstance places the geological setting either in a supra-subduction continental margin or in a subcontinental mantle-plume system. In the first case, the ultimate origin for the metasomatic fluids would be mostly crustal, derived from dehydration and partial melting of the sediments and oceanic crust of the subducting slab, whereas in the second case it would be of juvenile mantle origin.

Sr and Nd isotopes are inconclusive for deciding between these two possible geodynamic settings, as they are in the range of the majority of mantle-derived melts from subcontinental areas, regardless of their setting. The S isotopes, however, seem to exclude any contribution

of a source other than the mantle. The negative Nb and Ti anomalies, in contrast, could be symptomatic of subduction-related magmatism (e.g. Kelemen *et al.*, 1993; Davidson, 1996), although this idea is difficult to reconcile with the high enrichment in Zr and Hf, the extremely high variations in Zr/Nb, and with the consistently low Nb/Ta (Fig. 3), lower than expected for arc magmas, especially for those most enriched in incompatibles (Stolz *et al.*, 1996). Moreover, the pipes frequently have a positive Eu anomaly, a feature very common in the gabbros of the Basic Complex (e.g. Sinigoi *et al.*, 1994), but seldom found in subduction-related melts. We therefore conclude that, although not decisive, the whole geochemical picture is more in accordance with a mantle origin for the metasomatic agent.

Additional evidence favouring this supposition derives from the nature and composition of the hydrous silicates and accessory mineral assemblage of the pipes, which show an extraordinary similarity to the MARID (mica, amphibole, rutile and diopside) and the IRPS (ilmenite, rutile, phlogopite and sulphide) suites of minerals typical of metasomatized mantle xenoliths from kimberlites (Harte *et al.*, 1987; Haggerty, 1995), as well as to the primary carbonate-bearing pockets in fluid-metasomatized peridotite xenoliths described by Ionov (1998). The mineral assemblage of the pipes is indicative of a fluid phase rich in H_2O and CO_2, with significant P, S, F and Cl contents, notably similar to the composition of mantle metasomatic fluids inferred from the study of xenoliths by Erlank *et al.* (1987). Fluids with a similar composition are also resident in the primitive subcontinental mantle, and can produce alkaline silicate melts by very low-degree melting at the root or in the core of intra-continental mantle plumes (Watson *et al.*, 1990). These melts may have been extracted from the core of the plume, rapidly reaching the surface, with no significant wall-rock reaction, to form carbonatite–alkaline complexes (Moore & Wood, 1998). However, if they were retained in the depleted top of the mantle plume and had the chance to react with the residual harzburgite country rocks, they might have produced small amounts of high-Mg melts with an alkaline signature similar to that of the pipe magma.

Relationships with mantle metasomatism in the Ivrea Zone

The Finero massif represents an important example of mantle metasomatism in the Ivrea Zone (Cawthorn, 1975; Hartmann & Wedepohl, 1993; Garuti *et al.*, 1997, 1998; Lu *et al.*, 1997; Zanetti *et al.*, 1999). The mantle of Finero consists of flushed harzburgite characterized by a highly residual assemblage (olivine, orthopyroxene, chromite) and modal metasomatic re-enrichment in phlogopite and amphibole, with local carbonates, apatite and

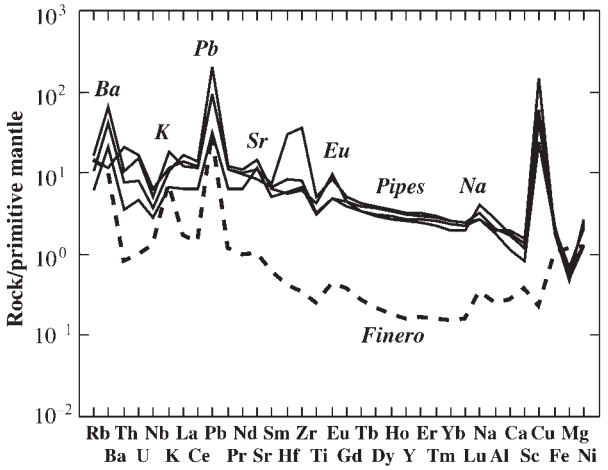

Fig. 10. Mantle-normalized trace-element patterns for the averages of the pipes (continuous lines) and the metasomatized peridotites (dashed line) of Finero (unpublished data of the authors, 1996). The similar anomalies in many incompatible elements should be noted. Values of the primitive mantle taken from McDonough & Sun (1995).

zircon (Ferrario & Garuti 1990). The metasomatic re-enrichment of the harzburgite may have started as a result of the interaction of the mantle protolith with upward-migrating fluid-rich melts about 293 $\pm$ 13 my ago (Voshage *et al.*, 1987), coeval with the intrusion of the pipes.

In addition to the similarities in age, the trace-element and Sr–Nd–S isotope geochemistry show striking affinities that suggest they could be closely connected. Figure 10 reveals that the trace-element pattern of the metasomatized peridotites (unpublished data of the authors, 1996; see also Hartmann & Wedepohl, 1993) parallels those of the pipes and has the same positive anomalies in Ba, K, Pb, Sr, Eu and Na. The main difference arises in the lack of a Cu anomaly as a result of the lower contents in S and other chalcophile elements in the peridotites. The distribution of Os–Ir–Ru–Rh–Pt is complementary to that of the pipes and also shows an important positive anomaly in Au and, to a lesser extent, in Pd (Fig. 11). Finally, in the $\varepsilon_{290\,Ma}(Nd)$ vs $\varepsilon_{290\,Ma}(Sr)$ diagram (Fig. 9), the pipes plot between the unmetasomatized and metasomatized peridotites, defining a continuous trend. All these data suggest a common origin for the agents that caused the metasomatic events in the pipes and in Finero.

In a recent paper, Zanetti *et al.* (1999) illustrated the effects of metasomatism at Finero and proposed that the metasomatizing fluids derived from a subducted slab active during the Variscan [see also Exley *et al.* (1982) and Hartmann & Wedepohl (1993)], a conclusion completely at odds to what we propose for the pipes, i.e. fluids derived from a mantle plume. A few considerations about the geological setting may shed some light on this subject.

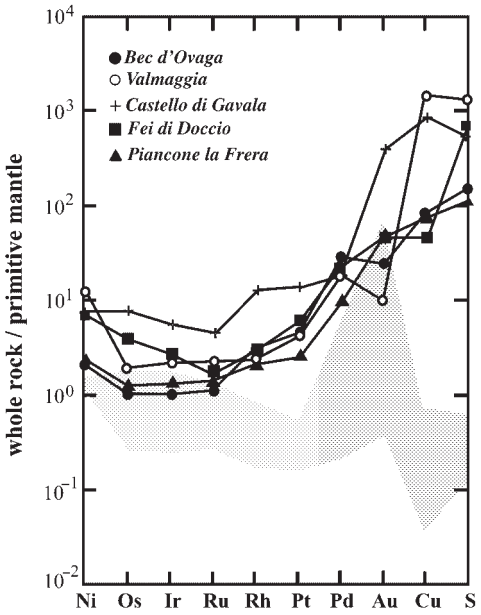

Fig. 11. Mantle-normalized plot for PGE, Au, Ni, Cu and S comparing the average patterns of the ultramafic pipes with the field of the Finero fluid-metasomatized residual mantle. Finero data from Garuti *et al.* (1997, 1998). Normalization values are from Barnes *et al.* (1988).

There is neither tectonic nor petrological evidence for a subduction system in the Southern Alpine domain of the Alps during the late Palaeozoic. Even the Permian high-K calc-alkaline magmatism of the central–eastern Southern Alps, which bears some resemblance to arc-magmatism, has been interpreted as originating by upwelling of hot asthenosphere in a regime of extension and thinning of the sub-continental lithosphere (Rottura *et al.*, 1998). Subduction-related mafic–ultramafic bodies are well known in other parts of the world, forming what is usually known as the Alaskan-type ultramafic bodies. A good example of a late Carboniferous subduction belt occurs in the Urals, where concentrically zoned dunite–clinopyroxenite–gabbro bodies with an age comparable with Finero form the backbone of the Platinum-Bearing Belt (e.g. Fershtater *et al.*, 1997). These massifs are spatially and temporally related to voluminous subduction-related calc-alkaline plutonism, ophiolites and accretionary terrains with exhumed high-P complexes (e.g. Zonenshain *et al.*, 1990), typical of palaeo-subduction orogens. Nothing of this nature exists in the Ivrea Zone. Here, a copious tholeiitic magmatism underplated—or was emplaced into—the lower continental crust as a result of the diapiric rise of discrete mantle plumes, probably triggered by extensional thinning of the lithosphere during late Variscan times (Shervais & Mukasa, 1991; Henk *et al.*, 1997). This led to a high-T regime, extremely unusual in subduction environments (e.g. Peacock, 1990), which resulted in extensive migmatization and granulite facies metamorphism. Therefore, despite the lack of conclusive evidence favouring either hypothesis, we consider that the mantle-plume alternative is more consistent with the chemical and mineralogical composition of the materials involved and with the geological setting.

Taking into account all available evidence, we propose that the Finero body could represent the final evolutionary stage of the metasomatized mantle plume from which the pipe magma was extracted. After the melting event(s) that produced the Basic Complex and depleted the plume material in incompatible elements, some parts of the plume underwent considerable contamination with alkaline fluids rising from below and locally producing the pipe magmas, which were extracted and injected upwards into the crust during the late Carboniferous. This metasomatized mantle, currently exposed at Finero, experienced a progressive equilibration with the contaminant until it was emplaced into the crust, possibly in the late Permian (Zanetti *et al.*, 1999).

CONCLUSIONS

The petrological, geochemical and geochronological data of the ultramafic pipes presented in this paper indicate that high-Mg, hydrous magmas enriched in volatiles and incompatible elements with an alkaline signature were produced by mantle metasomatism of a depleted source, and then intruded into the deep crust of the Ivrea Zone during the late Carboniferous (287 $\pm$ 3 Ma).

The intrusion of the pipes probably represents the last magma pulse marking the end of the mantle magmatism in the cross-section of Valsesia. The similarity in chemical composition, isotopic signature and age indicates that the pipes were produced in the course of the same metasomatic event that affected the Finero body, whose metasomatized peridotites represent the final evolutionary stage of the metasomatized mantle plume.

The mineralogy, trace-element geochemistry and S isotopic composition of the pipes does not support a crustal origin for the metasomatic fluids. We therefore suggest that they had a juvenile mantle origin and were probably generated by very low-degree melting at the root or in the core of the subcontinental mantle plume that caused the underplating event in Ivrea.

ACKNOWLEDGEMENTS

We are indebted to M. Wilson, B. Upton, E. A. Dunworth and an anonymous referee for their helpful comments and suggestions, which greatly contributed to improving the manuscript. The help of Christine Laurin with the English is gratefully acknowledged. This work has been

funded by the Italian MURST and the Spanish DGICYT (Joint Action No. HI-0110). Laboratory expenses at the University of Granada were also supported by DGICYT grants PB96-1266 and PB98-1345.

REFERENCES

Barnes, S. J., Boyd, R., Korneliusson, A., Nilsson, L. P., Often, M., Pedersen, R. B. & Robins, B. (1988). The use of mantle normalization and metal ratios in discriminating between the effects of partial melting, crystal fractionation and sulphide segregation on platinum-group elements, gold, nickel and copper: examples from Norway. In: Prichard, H. M., Potts, P. J., Bowles, J. F. W. & Cribb, S. J. (eds) *Geo-platinum 87*. Barking, UK: Elsevier Applied Science, pp. 113–143.

Bea, F. (1996). Controls on the trace element composition of crustal melts. *Transactions of the Royal Society of Edinburgh: Earth Sciences* **87**, 33–42.

Bea, F. & Montero, P. (1999). Behavior of accessory phases and redistribution of Zr, REE, Y, Th, and U during metamorphism and partial melting of metapelites in the lower crust: an example from the Kinzigite Formation of Ivrea–Verbano, NW Italy. *Geochimica et Cosmochimica Acta* **63**, 1133–1153.

Bertolani, M. (1952). Studio microscopico a luce riflessa sui minerali dei giacimenti cupro-nicheliferi della Val Sesia. *Rendiconti della Società Italiana di Mineralogia e Petrografia* **8**, 67–86.

Bertolani, M., Capedri, S. & Loschi Ghittoni, A. G. (1980). Mineralizzazione a solfuri di un'ultramafite della Val Sessera (Vercelli). *Bollettino della Associazione Mineraria Subalpina* **3–4**, 576–586.

Boriani, A., Burlini, L. & Sacchi, R. (1990). The Cossago–Mergozzo–Brissago Line and the Pogallo Line (Southern Alps, Northern Italy) and their relationships with the late-Hercynian magmatic and metamorphic events. *Tectonophysics* **182**, 91–102.

Cawthorn, R. G. (1975). The amphibole peridotite–metagabbro complex, Finero, Northern Italy. *Journal of Geology* **83**, 437–454.

Davidson, J. P. (1996). Deciphering mantle and crustal signatures in subduction zone magmatism. In: Bebout, G. E., Scholl, D. W., Kirby, S. H. & Platt, J. P. (eds) *Subduction. Top to Bottom. Geophysical Monograph, American Geophysical Union* 96, 251–262.

Erlank, A. J., Waters, F. G., Hawkesworth, C. J., Haggerty, S. E., Allsopp, H. L., Rickard, R. S. & Menzies, M. A. (1987). Evidence for mantle metasomatism in peridotite nodules from the Kimberley pipes, South Africa. In: Menzies, M. A. & Hawkesworth, C. J. (eds) *Mantle Metasomatism*. London: Academic Press, pp. 221–311.

Exley, R. A., Sills, J. D. & Smith, J. V. (1982). Geochemistry of micas from the Finero spinel-lherzolite, Italian Alps. *Contributions to Mineralogy and Petrology* **81**, 59–63.

Ferrario, A. & Garuti, G. (1990). Platinum-group mineral inclusions in chromitites of the Finero mafic–ultramafic complex (Ivrea-Zone, Italy). *Mineralogy and Petrology* **41**, 125–143.

Ferrario, A., Garuti, G. & Sighinolfi, G. P. (1982). Platinum and palladium in the Ivrea–Verbano basic complex, western Alps, Italy. *Economic Geology* **77**, 1548–1555.

Fershtater, G. B., Montero, P., Borodina, N. S., Pushkarev, E. V., Smirnov, V. N. & Bea, F. (1997). Uralian magmatism: an overview. *Tectonophysics* **276**, 87–102.

Garuti, G. & Rinaldi, R. (1986). Melonite-group and other tellurides from the Ivrea–Verbano basic complex, western Italian Alps. *Economic Geology* **81**, 1213–1217.

Garuti, G. & Zaccarini, F. (1994). I minerali del gruppo del platino: primi ritrovamenti in Italia. *Atti della Società dei Naturalisti e Matematici di Modena* **125**, 11–28.

Garuti, G., Fiandri, P. & Rossi, A. (1986). Sulphide composition and phase relations in the Fe–Ni–Cu ore deposits of the Ivrea–Verbano basic complex (western Alps, Italy). *Mineralium Deposita* **21**, 22–34.

Garuti, G., Naldrett, A. J. & Ferrario, A. (1990). Platinum-group elements in magmatic sulphides from the Ivrea Zone: their control by sulphide assimilation and silicate fractionation. *Economic Geology* **85**, 328–336.

Garuti, G., Oddone, M. & Torres-Ruiz, J. (1997). Platinum-group element distribution in subcontinental mantle: evidence from the Ivrea-Zone (Italy) and the Betic–Rifean cordillera (Spain and Morocco). *Canadian Journal of Earth Science* **34**, 444–463.

Garuti, G., Rivalenti, G., Rossi, A., Siena, F. & Sinigoi, S. (1980). The Ivrea–Verbano mafic ultramafic complex of the Italian western Alps: discussion of some petrologic problems and a summary. *Rendiconti della Società Italiana di Mineralogia e Petrografia* **36**, 717–749.

Garuti, G., Zaccarini, F., Montero, P. & Bea, F. (1998). Platinum-group element and gold metasomatism in the Earth's mantle as illustrated by PGE–REE–Incompatible Elements relationships in orogenic lherzolite massifs of the Ivrea Zone (Italy). In: *8th International Pt Symposium, 28 June–3 July 1998, Abstracts*. Johannesburg: South African Institute of Mining and Metallurgy, pp. 121–124.

Govindaraju, K., Potts, P. J., Webb, P. C. & Watson, J. S. (1994). 1994 Report on Whin Sill Dolerite WS-E from England and Pitscurrie Micrograbbro PM-S from Scotland: assessment by one hundred and four international laboratories. *Geostandards Newsletter* **18**, 211–300.

Green, T. H. (1995). Significance of Nb/Ta as an indicator of geochemical processes in the crust–mantle system. *Chemical Geology* **120**, 347–359.

Haggerty, S. E. (1995). Upper mantle mineralogy. *Journal of Geodynamics* **20**, 331–364.

Harte, B., Winterburn, P. A. & Gurney, J. J. (1987). Metasomatic and enrichment phenomena in garnet peridotite facies mantle xenoliths from the Matsoku Kimberlite pipe, Lesotho. In: Menzies, M. A. & Hawkesworth, C. J. (eds) *Mantle Metasomatism*. London: Academic Press, pp. 145–220.

Hartmann, G. & Wedepohl, K. H. (1993). The composition of peridotite tectonites from the Ivrea Complex, northern Italy: residues from melt extraction. *Geochimica et Cosmochimica Acta* **57**, 1761–1798.

Henk, A., Franz, L., Teufel, S. & Oncken, O. (1997). Magmatic underplating, extension, and crustal reequilibration: insights from a cross-section through the Ivrea Zone and Strona–Ceneri Zone, northern Italy. *Journal of Geology* **105**, 367–377.

Hofmann, A. W. (1988). Chemical differentiation of the Earth: the relationship between mantle, continental crust, and oceanic crust. *Earth and Planetary Science Letters* **90**, 297–314.

Huttenlocher, F. (1934). Die Erzlagerstättenzonen der Westalpen. *Schweizerische Mineralogische und Petrographische Mitteilungen* **14**, 22–149.

Ionov, D. (1998). Trace element composition of mantle-derived carbonates and coexisting phases in peridotite xenoliths from alkali basalts. *Journal of Petrology* **39**, 1931–1941.

Johnson, R. & Bhattacharyya, G. (1984). *Statistics. Principles and Methods*. New York: John Wiley, 578 pp.

Kelemen, P. B., Shimizu, N. & Dunn, T. (1993). Relative depletion of niobium in some arc magmas and the continental crust: partitioning of K, Nb, La and Ce during melt/rock reaction in the upper mantle. *Earth and Planetary Science Letters* **120**, 111–134.

Kober, B. (1986). Whole-grain evaporation for $^{207}Pb/^{206}Pb$-age investigations on single zircons using a double filament thermal

ionization source. *Contributions to Mineralogy and Petrology* **93**, 482–490.

Kober, B. (1987). Single-zircon evaporation combined with Pb^+ emitter-bedding for $^{207}Pb/^{206}Pb$ age investigations using thermal ion mass spectrometry and implications to zirconology. *Contributions to Mineralogy and Petrology* **96**, 63–71.

Le Maitre, R. W. (1982). *Numerical Petrology*. Amsterdam: Elsevier, 281 pp.

Lu, M. H., Hofmann, A. W., Mazzucchelli, M. & Rivalenti, G. (1997). The mafic–ultramafic complex near Finero (Ivrea–Verbano Zone). 1 *Chemistry of MORB-like Magmas*. *Chemical Geology* **140**, 207–222.

McDonough, W. F. & Sun, S. S. (1995). The composition of the Earth. *Chemical Geology* **120**, 223–253.

Mehnert, K. R. (1975). The Ivrea Zone, a model of the deep crust. *Neues Jahrbuch für Mineralogie, Abhandlungen* **125**, 156–199.

Montero, P. & Bea, F. (1998). Accurate determination of $^{87}Rb/^{86}Sr$ and $^{147}Sm/^{144}Nd$ ratios by inductively-coupled-plasma mass spectrometry in isotope geoscience: an alternative to isotope dilution analysis. *Analytica Chimica Acta* **358**, 227–233.

Moore, K. R. & Wood, B. J. (1998). The transition from carbonate to silicate melts in the $CaO–MgO–SiO_2–CO_2$ system. *Journal of Petrology* **39**, 1943–1951.

Naldrett, A. J. (1989). *Magmatic Sulphide Deposits*. New York: Oxford University Press, 196 pp.

Peacock, S. M. (1990). Numerical simulation of metamorphic pressure–temperature–time paths and fluids production in subducting slabs. *Tectonics* **9**, 1197–1211.

Percival, J. A., Fountain, D. M. & Salisbury, M. H. (1992). Exposed crustal cross sections as windows on the lower crust. In: Fountain, D. M., Arculus, R. & Kay, R. W. (eds) *Continental Lower Crust. Developments in Geotectonics, 23*. Amsterdam: Elsevier, pp. 317–362.

Pin, C. (1986). Datation U–Pb sur zircons à 285 Ma du complexe gabbro–dioritique du Val Sesia–Val Mastallone et âge tardi-hercynien du métamorphisme granulitique de la Zone Ivrea–Verbano (Italie). *Comptes Rendus de l'Académie des Sciences, Série II* **303**, 827–830.

Pin, C. & Sills, J. D. (1986). Petrogenesis of layered gabbros and ultramafic rocks from Val Sesia, the Ivrea Zone, NW Italy: trace element and isotope geochemistry. In: Dawson, J. B., Carswell, D. A., Hall, J. & Wedepohl, K. H. (eds) *The Nature of the Lower Continental Crust. Geological Society, London, Special Publication* **24**, 231–249.

Rogers, J. J. W. & Adams, J. A. S. (1969). Uranium. In: Wedepohl, K. H. (ed.) *Handbook of Geochemistry*. Heidelberg: Springer, pp. II–5.

Rottura, A., Bargossi, G. M., Caggianelli, A., Del Moro, A., Visonà, D. & Tranne, C. A. (1998). Origin and significance of the Permian high-K calc-alkaline magmatism in the central–eastern Southern Alps, Italy. *Lithos* **45**, 329–348.

Schnetger, B. (1994). Partial melting during the evolution of the amphibolite- to granulite-facies gneisses of the Ivrea Zone, northern Italy. *Chemical Geology* **113**, 71–101.

Shervais, J. W. & Mukasa, S. B. (1991). The Balmuccia orogenic lherzolite massif, Italy. *Journal of Petrology, Special Lherzolite Issue* 155–174.

Sinigoi, S., Quick, J. E., Clemens-Knott, D., Mayer, A., Demarchi, G., Mazzuchelli, M., Negrini, L. & Rivalenti, G. (1994). Chemical evolution of a large mafic intrusion in the lower crust, Ivrea–Verbano Zone, northern Italy. *Journal of Geophysical Research* **99**, 21575–21590.

Stacey, J. S. & Kramers, J. D. (1975). Approximation of terrestrial lead isotope evolution by a two-stage model. *Earth and Planetary Science Letters* **26**, 207–221.

Stolz, A. J., Jochum, K. P., Spettle, B. & Hofmann, A. W. (1996). Fluid- and melt-related enrichment in the subarc mantle: evidence from Nb/Ta variations in island-arc basalts. *Geology* **24**, 587–590.

Systat (1992). *Statistics Version 5·2*. Evanston, IL: Systat, Inc., 724 pp.

Tredoux, M., Lindsay, N. M., Davies, G. & Housley, R. M. (1995). The fractionation of platinum-group elements in magmatic systems, with the suggestion of a novel causal mechanism. *South African Journal of Geology* **98**, 157–167.

Voshage, H., Hunziker, J. C., Hofmann, A. W. & Zingg, A. (1987). A Nd and Sr isotopic study of the Ivrea zone, Southern Alps, N Italy. *Contributions to Mineralogy and Petrology* **97**, 31–42.

Watson, E. B., Brenan, J. M. & Baker, D. R. (1990). Distribution of fluids in the continental mantle. In: Menzies M. A. (ed.) *Continental Mantle. Oxford Monographs on Geology and Geophysics 16*. Oxford: Oxford University Press, pp. 111–125.

Wyllie, P. J. (1995). Experimental petrology of upper mantle materials, process and products. *Journal of Geodynamics* **20**, 429–468.

Zanetti, A., Mazzucchelli, M., Rivalenti, G. & Vannucci, R. (1999). The Finero phlogopite–peridotite massif: an example of subduction-related metasomatism. *Contributions to Mineralogy and Petrology* **134**, 107–122.

Zonenshain, L. P., Kuzmin, M. I. & Natapov, L. M. (1990). Geology of the USSR: a plate-tectonics synthesis. In: Page, B. M. (ed.) *Geology of the USSR: a Plate-Tectonics Synthesis. Geodynamic Series, American Geophysical Union* **21**, 27–54.